STUDY OF IMPULSE CHARACTERISTICS

INDUCED BY REPETITIVE LASER PULSE ABLATION

（繰返しパルスレーザー照射によるアブレーション力積特性に関する研究）

BY
HISASHI TSURUTA

DEPARTMENT OF AEROSPACE ENGINEERING
NAGOYA UNIVERSITY

June 2017

Contents

List of Tables

List of Figures

Nomenclature

A = amplitude, V

B = output signal of linear variable differential transformer, V

C = damping coefficient

C_m = momentum coupling coefficient, Ns/J

D_c = crater diameter, m

E = laser energy, J

E_t = total laser energy, J

E_p = energy of single laser pulse, J

f = laser pulse repetition frequency, Hz

g = gravitational acceleration, m/s^2

g_e = ratio represent the decreament of maximum deflection caused by τ_L

h = crater depth, m

h_s = slant height of corn, m

I = radiation intensity, W/m^2

I_m = impulse, Ns

$I_{m,i}$ = impulse induced by ith laser pulse, Ns

J = angular momentum of inertia, kgm^2

K = restoring force, Nm

m = ablated mass, kg

M^2 = M square

N_t = total number of laser pulses

$N_{t,1}$ = initial total pulse number in averaging

$N_{t,2}$ = end total pulse number in averaging

N_b = number of laser pulses within a burst

$\overline{N}_t$ = averaged pulse number

p = pressure, N

R = reflectance

r_L = radial location of laser pulse irradiation, m

S = ablation spot area, m^2

S_i = area with diameter of D_c, m^2

S_l = lateral area of circular cone, m^2

T_a = effective transmittance during ablation

T_i = transmittance without ablation

t = time, s

t_0 = initiation time of laser pulse irradiation, s

I = radiation intensity, W/m^2

$\overline{v}$ = mass-averaged exhaust velocity, m/s

v_e = exhaust velocity, m/s

x = material thickness, m

x_a = ablation depth, m

α_a = effective absorption coefficient during ablation, 1/m

α_i = absorption coefficient without ablation, 1/m

α_s = aspect ratio

β = coupling of I_m divided by A, Ns/V

η = energy efficiency

$\overline{\eta}$ = averaged energy efficiency

θ = deflection angle, degrees

λ = wavelength, m

μ = exhaust mass areal density by laser ablation, kg/m^2

ρ = density, kg/m^3

τ = laser pulse duration time, full width at half maximum, s

τ_0 = natural oscillation period of pendulum, s

τ_L = temporal impulse duration, s

$\Delta\tau_L$ = time interval between successive laser pulses, s

ϕ_e = effective fluence, J/m^2

ϕ_p = single pulse fluence, J/m^2

ϕ_t = threshold fluence, J/m^2

ψ = constant in Eq. 3.4

ω = angular velocity of torsion pendulum arm, rad/s

Chapter 1.
Introduction

1.1 Background

1.1.1 Problem in space activities

The amount of space debris is rapidly increasing due to swift expansion of space development activities. While space debris fragmentation is rapidly proceeding, the number of debris larger than 1 cm is also increasing, being estimated to exceed 600,000 and peaks at an orbital altitude of 800 km. While the relative collision velocity of the debris is at a level of 10 km/s, the satellites, space station, and so on can be seriously damaged because of collisions with even the small-sized debris. Moreover, according to “Kessler Syndrome” [1], the amount of debris will increase owing to fragmentation caused by mutual collisions. Debris below 1 cm in diameter are shielded by the debris shield mounted on the satellite, whereas debris larger than 10 cm are tracked by the debris tracking system, which sends an alert, so that the satellite can avoid a collision. Therefore, debris within the diameter range of 1 cm to 10 cm is the most dangerous. This is because the momentum of the impact exceeds the ability of the debris shield to withstand collisions. Moreover, this type of debris is large in quantity and difficult to find and track, using ground-based telescopes.

Future missions with geodetic or astronomic science goals require highly precise compensation of disturbing forces that prevent satellites from maintaining an ideal orbit or

interfere with satellite formation fight [2]. Depending on the mission, disturbing forces are atmospheric drag in low earth orbit (1 mN), solar radiation pressure of the order of 10 to 100 μN (the dominating effect in deep space), torques due to Earth magnetic field and for the case of satellite formation fight balance of tidal forces. For future developments for example earth observation missions that provide higher resolution even space craft dynamics have to be considered.

1.1.2 Survey of space propulsion methods

The electric propulsion thrusters have already been developed, and demonstrating to be functional in their practical applications. The typical range of the specific impulse (I_{sp}) for electric propulsion is 10^2–10^4 s, which is considerably higher than the 300 s for chemical propulsion. While the maximum thrust density of electric propulsion is an order of magnitude smaller than chemical propulsion, the thrust range is as wide as of 1–10^4 N/m^2. For micropropulsion, the FEEP (Field Emission Electric Propulsion) thruster with a specified thrust of 0.1–100 μN has been developed [3-5]. The main feature of the electric thruster is the high specific impulse range of 4000–10000 s[6], which is achieved because of a high applied voltage of about 10 kV. The disadvantage of FEEP is a heavier weight of power supply caused by high voltage. Moreover, a neutralizer for the ion beam is also required.

An electrodynamic tether [7,8] can work as a thruster because a magnetic field exerts a force on a current carrying wire. This force is perpendicular to the wire and to the geomagnetic field vector. If the current flows downward through a tether connected to an eastward-moving spacecraft, the force exerted by the geomagnetic field on the system has a component that accelerates the satellite along the direction in which it is already moving. The propulsion method does not require any propellant on board. The thrust generated by a tether of a length of 10 km was estimated to be in the range of 0.3–1.2 N with an input power in the range of 0.3–1.5 kW. A

smaller thrust can be obtained by shortening the tether length or by decreasing the input power. Although the use of electric propulsion is not necessary within a region such a low Earth orbit where the geomagnetic field is sufficiently strong, the deformation of the tether wire may cause a difficult in obtaining a stable thrust.

The typical I_{sp} of laser ablation propulsion is in the range of 200–3000 s. [9] The thrust density is on the order of 8×10^5 N/m^2 [10], because the thrust arises on a spot with an area equal to that of a focused laser beam. Remote thrust generation is a unique and clear advantage of this technique. It has the potential to achieve significant mass reduction and improved payload capability. The use of solid propellant alleviates problems in propellant storage. The thrust is roughly proportional to the laser power. Therefore, the system size can be scalable to a required thrust. However, regardless of such advantages, this propulsion technique has not been matured for practical applications.

1.1.3 Laser ablation propulsion

Laser ablation is the mass removal of target material by using laser energy. The material surface absorbs the laser energy, heats it up rapidly, and then ejects the materials basically in its gas phase. Laser ablation propulsion utilizes the recoil force of the ejection as a thrust. Its remote thrust generation is a unique and important advantage of this technique. Various materials can be ablated and imparted impulse by laser ablation. The impulse level can be controlled by laser irradiation conditions including a laser pulse energy, an energy density, the number of laser pulses etc.

The application of laser propulsion is a promising solution to the space debris problem. Laser ablation is capable of treating space debris at distances within 100 km. Thus, the operation can be conducted safely without the risk of collision with the debris. Moreover, multiple occurrences of the debris can be de-orbited by a single laser source. This feature is suitable for treating small

type of debris, whose amount exceeds 600,000 and is spread over a large space.

Microthrusters [11,12] driven by the laser ablation are promising candidate for the future space mission which require small and highly precise thrust. Depending on the ablation threshold of the target material different approaches are possible: Diode lasers with relatively long pulses in the ms range have been used for ablation of polymer targets in transmission or T-mode, where the thin target is located on a transparent substrate [13]. The laser pulse transmit the substrate and then be absorbed by the target. The induced pressure acts on the substrate is in the direction of opposite of the laser direction. In this concept a fresh spot of coated material has to be provided for each shot. Microchip lasers that produce shorter pulses can be used for reflection or R-mode ablation of metal targets. The laser pulse is directly irradiated onto the metal target. This mode have a higher ablation threshold but are not subject to outgassing issues like polymer targets. Thrust levels between mN and μN have been demonstrated for laser ablative thrusters. Specific impulses of up to more than 3000 s have been demonstrated for R- mode metal ablation [14,15] and impulse coupling coefficients of up to 3000 μNs/J have been demonstrated in T-mode ablation of exothermic polymers [12]. A unique capability of laser ablative thrusters is the generation of very low minimum impulse bits down to < 1 nNs in a single shot operation [15,16].

1.2 Review of research and development

1.2.1 Space debris mitigation

Active removal of debris is studied in many research institutes such as JAXA [17,18], ESA [19], and NASA [20-22]. Almost all the methods of debris removal have to approach and contact to the debris. However, the collision risk involved in and the fuel expenditure required for approaching the debris accompanies. These studies address single pieces of debris larger than 1 m. This is because large pieces of debris give rise to many smaller pieces of debris by collision

with other debris. However, the spatial density of small debris has already a non-negligible level. For example, the International Space Station executes a collision avoidance maneuver about once a year. Therefore, development of active deorbiting method both for large and small debris is important to maintain safety on Earth's orbits.

The application of laser propulsion is one promising solution to this problem. Phipps et al. [23] advocated the concept of deorbiting space debris in low Earth orbit by using a 20 kW laser device located on the ground. On the other hand, space debris mitigation by space based deployment of the laser as shown in Figure 1.1 have been energetically studied. Schall et al. [24] proposed this concept. A power higher than 1 kW with an about 40 % efficiency laser system named CAN (Coherent Amplifying Network) has been developed for space debris removal in orbit [25]. The system adopts a high operation repetition rate of more than 1 kHz with a constant fluence. It was reported that debris of $1 - 10$ cm in size can be de-orbited with this laser system. Although a constant momentum coupling coefficient, C_m is used in their estimation, the actual C_m would change in repetitive laser pulse irradiations. The ablation phenomenon with repetitive irradiation is more complicated than single-pulse irradiation onto a planer ablator because the condition of a crater which is formed during the laser pulse irradiations influences the total impulse. Ebisuzaki et al. [26] embodied these concepts by utilizing the Extreme Universe Space Observatory (EUSO) and CAN fiber laser. De-tumbling of an artificial satellite model through the use of repetitive laser pulses was demonstrated in [27].

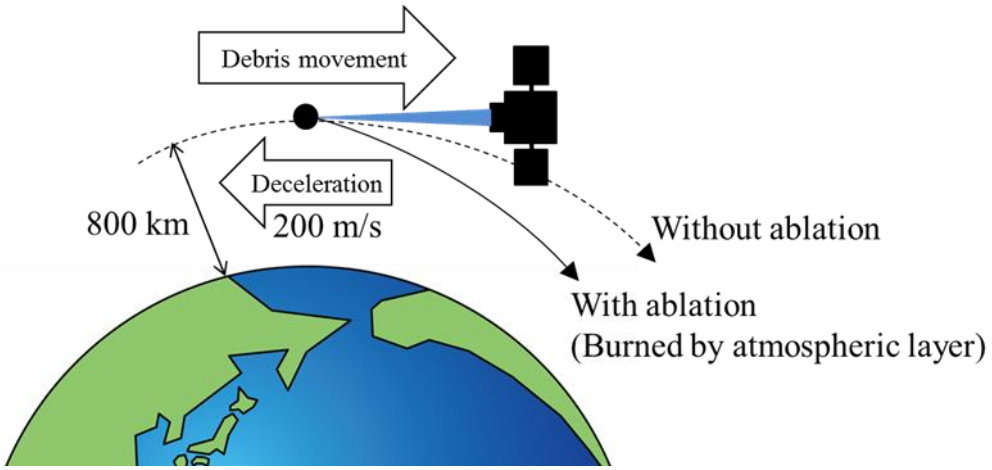

Figure 1.1 Conceptual drawing of space debris mitigation by space based deployment of the laser.

1.2.2 Impulse generation by laser ablation

Previous research on laser ablation propulsion was mostly focused on the impulse performance obtained with a single laser pulse irradiation using a target with a flat surface and dimensions that were much larger than the laser beam diameter. The impulse mainly depends on the incident laser fluence, ϕ_p, which is the energy density in the illuminated area. Phipps, et al. [9] proposed a model to relate C_m, and ϕ_p based on existing data and theory, and concluded that the fluence had an optimum value to maximize C_m, the value of which is strongly dependent on ablation materials and laser pulse specifications. In their proceeding paper [28], they obtained the same impulse performance with 130 fs laser pulse as that with a 100 ps laser pulse. In most practical applications except for the micropropulsion, a sufficient impulse cannot be obtained with a single laser pulse irradiation.

A previous study [29] showed that C_m was proportional to $(I\lambda\sqrt{\tau})^{-1/4}$ under plasma regime; C_m increases with decreasing λ. To support this tendency, metals ablated by 532-nm-wavelength laser pulses exhibited promising propulsion performance [30]. However, at

the current technology level, a 1-μm-wavelength laser can reach higher output power and efficiency than those of its higher harmonics. Considering the 'overall' C_m, the ratio of a propulsive impulse to the input electrical energy to the whole system, the 1-μm-wavelength laser pulse still has an advantage over the higher harmonic waves. Souza [31] reported that with a femtosecond to picosecond level pulse duration laser, C_m is kept almost constant with the laser fluence, ϕ_p being varied in the range of 0.2 to1.6× J/cm^2. Impulse is not sensitive to f (5.0 – 6.5 kHz), N_t (100 – 3000 shots) and τ (100 – 940 ps). However, the main objective of work was to determine whether or not the pico-second pulse width offered a significant performance increase compared to nanosecond pulse width. A part of laser pulse width in his experiment is shorter than the plasma formation timescale, on the order of 1 – 10 ps. It is unknown if this pulse width range is useful for space propulsion applications or not.

1.2.3 Laser devices

There has been tremendous improvement in the recent performance of the diode laser. The commercial pulse laser by Quantel Co. generates up to 1 MW power with up to 65% efficiency and guarantees operation in space. The high efficiency helps in saving electric power, which is especially valuable in space, and in lowering heat generation. Moreover, because of the small volume, the cost of manufacturing, launching, and operation can be reduced. A laser system with efficiency of nearly 40 % and power more than 1 kW has been developed for the removal of space debris in the Earth's orbit [25]. The system adopts a high laser repetition rate of more than 1 kHz with a constant ϕ_p. It was reported that debris of 1 – 10 cm in size, at a distance of 100 km, was de-orbited with this laser system.

1.3 Specific research problems

1.3.1 Generation of required impulse

The minimum impulse induced by single pulse ablation is < 1 nNs and it satisfies most of the requirements for a small impulse. In the meantime, there is a limitation for the maximum impulse with single pulse ablation. Impulse, I_m generated on the object surface by laser ablation can be expressed as the multipullcation of laser energy, E by C_m,

$$I_m = EC_m \tag{1.1}$$

The equation also gives the definition of C_m, which is the thrust effectiveness from laser energy to the impulse. In debris removal operation, there is a certain limitation on E mainly due to the limited debris surface area and the distance, so the C_m should be sufficiently high for obtaining enough impulse. Several authors have reported that C_m increased to the peak value and then decreased while increasing the fluence of the laser pulse, [9]. Therefore, the impulse generated with single pulse is insufficient for operation.

Repetitive irradiation of the laser pulse is useful for obtaining a sufficient impulse for practical use. Repetitive irradiation with a total number (N_t) of laser pulses and laser pulse repetition frequency f can affect the impulse. However, this has not yet been studied. Even due to ablation by a single pulse, the ablator surface undergoes slight deformation and the surface area changes. Moreover, the surface roughness and reflectivity also change. These elements continuously vary with increasing N_t. When f increases beyond a certain value, the second pulse is arrived before the ablator surface temperature once rose with the first pulse decreases to ordinary

value. Under this condition, although the oscillations synchronize with f [32], the ablator temperature increases to the boiling point within several pulses and then remains constant. This may decrease the effective ablation threshold in the fluence, because the absorbed energy is not utilized for increasing the temperature. Double-laser-pulse impulse performance was reported by some authors: Colao, et al. [33] measured the emission spectrum of pulsed laser generated plasma. Using a Nd:YAG laser (wavelength 1064 nm, pulse width 8 ns) higher plasma density was obtained in 'double pulse' operation with 20 ms of pulse to pulse period than in single pulse operation even with an equal total energy. Mori et al. [34] reported the C_m enhancement effect by preheating the ablator before ablation. When f increases further, the plasma, gas, liquid, and solid particles exhausted by a previous pulse may remain near the ablated surface with non-negligible density and interfere with the next pulse resulting in a decrease in I_m.

For accomplishing constant impulse, even with repetitive irradiation, Phipps [12,28] developed a microthruster in which an ablator is fed as a roll of double layer tape, the layer on the irradiation side is transparent to the laser beam, the other side an ablator. The laser energy deposition is done on a virgin layer so that a single pulse performance is reproduced in every shot. However, this method is feasible only if an object to be propelled is a controllable one like a spacecraft, not applicable for an uncontrollable object such as space debris; even for a thruster in a spacecraft, the ablator utilization efficiency is degraded by the mass of the transparent layer and a dead area without irradiation.

The aerodynamic nozzle is another approach for enhancing impulse. The nozzle can be designed and attached to the thruster in advance. Sinko et al. [35] ablated carbon-doped polyoxymethylene POM in a set of conical aluminium (Al) mini-thrusters using a carbon dioxide (CO_2) laser. The laser had a pulse length of 300 ns, operating wavelength of 10.6 μm, and pulse energy in the range 1–4 J at standard temperature and pressure. I_m, C_m, and I_{sp} all increased with increasing expansion ratio, but the ablated mass per area appeared to remain

approximately constant. These results imply that the addition of the thruster nozzle to the target does not change the ablation mechanism in the material, but does contribute additional thrust through the action of the exhaust pressure. The crater, which formed and deepened with repetitive ablation, could act as the nozzle. Suzuki, et al. [36] investigated the impulse performance of TEA (Transversely-Excited Atmospheric) CO_2 laser pulses onto polyoxymethylene (POM) with a repetition frequency of 50 Hz and up to 110 pulses. Under favorable conditions (ambient pressure; 10^{-2} Pa, single pulse fluence; 18.8× J/cm^2), C_m increased by 8 % after 100 pulses, due to the formation of a crater which acted as a nozzle. However, with an excessively high fluence, the C_m decreased when the depth to diameter ratio of the crater exceeded unity.

1.3.2 Ablator materials

In recent years, the impulse performance, which acts as a laser ablation propulsion propellant, of polymer ablation has been studied [39-42]. A variety of polymers are utilized in space applications such as thermal control components, electronics related components, composites for structural applications, and adhesives[43]. Generally, polymers have lower latent heats for melting and vaporization than metals, thereby ejecting a larger mass and generating larger impulses induced by laser ablation. Therefore, polymers are quite important for laser ablation applications in space propulsion such as space debris deorbiting[25,44,45], dead satellite de-tumbling to capture, and microthruster[2,11]. From the viewpoint of propellant, suitable machinability, low density, and reasonable price of polymers are advantage. In addition, functionalization by blending and lamination has been examined. Many reported that polyoxymethylene (POM) acted as a volume absorber [46] against a far-infrared 10.6 μm CO_2 laser pulse, obtaining favorable impulse characteristics[47-49]. At the state of the art, a CO_2 laser can output a relatively large laser pulse energy, E_p. However, this typical gas dynamic laser system

is large, heavy, and has poor portability, thus is not suitable for the space applications. On the other hand, recent progresses in 1 μm high-repetition-rate solid-state lasers, including fiber lasers, are satisfactory in terms of energy conversion efficiency, weight, and cost. If a sufficient impulse performance is obtained with this type of laser device, the applicability of laser ablation in space propulsion is expected to be improved significantly.

Suzuki et al. [36] and Tsuruta et al. [50] examined the impulse characteristics by repetitively irradiating laser pulses on to a single spot. Colao et al. [33] measured the emission spectrum of a pulsed laser-generated plasma. Even with an equal amount of total energy, a higher plasma density was obtained using a Nd:YAG laser (wavelength, λ: 1064 nm, and a temporal pulse width, τ: 8 ns) in a double-pulse operation with a time interval of 20 ms than in a single-pulse operation. Mori et al.[34] preheated materials such as PVC, PMMA, and CFRP followed by laser ablation by CO_2 laser irradiation. As a result, the momentum coupling coefficient, C_m, which is the ratio of an impulse to a laser pulse energy irradiated on the ablator, of PMMA was increased by 20–40 μNs/J. Characteristics of I_m with high repetitive 1 μm laser irradiation have not yet been cleared, although they are essential for practical applications.

A summary of the principal parameters is shown in Figure 1.2. Although magnitude relation of D_{laser} and D_{target} and rotation of the ablator should influence on impulse, these parameters are beyond the scope of this study.

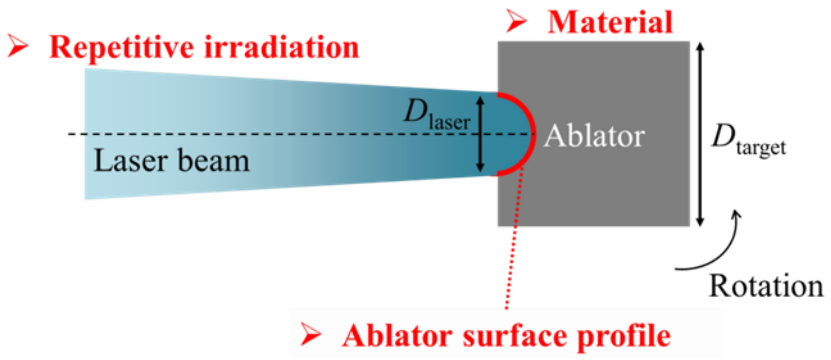

Figure 1.2 Principal parameters.

1.4 Objectives of this study

The objective of this study is to characterize an ablation impulse induced by repetitive laser pulse irradiations depending on laser operation and material conditions with understanding associated physical mechanisms.

Succeeding this chapter, first, apparatus and methods in the study are introduced in Chapter 2.

In Chapter 3, firstly, the impulse characteristics of an aluminum ablator against repetitive Nd:YLF laser pulses with 1047nm wavelength, 5 – 15 ns pulse width, are investigated. The laser is operated in burst modes with a varying pulse repetition frequency, single pulse energy and pulse number. The burst is repeated until impulse saturated. The fluence range is from 6 – 24 J/cm^2. A torsion pendulum is used to measure total impulse generated in a single burst with an accuracy of better than 2 % even with a burst period of one second. Influence of pulse repetition frequency, total laser pulse energy, and single pulse fluence are clarified. It becomes clear that formation and deepening of the crater affect the impulse characteristics of repetitive laser ablation. In addition, propulsion performance is reported through the exhaust mass measurement. Subsequently, impulse characteristics against larger energy pulses of Nd:YAG laser (wavelength of 1064 nm, pulse duration of 7 ns) is investigated. The fluence range is from 16 – 75 J/cm^2. Larger crater formed on the ablator is helpful for investigating the relationship between impulse and the crater profile. Surface area changes caused by crater deepening are measured with a laser microscope, then used for calculating the effective fluence. The fluence is compared to a corresponding variation in the momentum-coupling coefficient with repetitive pulses. Through the discussion, influence of the effective fluence on impulse will be revealed.

In Chapter 4, using the almost same setup of Chapter 3, the ablation spot area and impulse characteristics of various polymers are experimentally investigated against burst irradiation of

Nd:YLF laser pulses with a pulse repetition frequency of 1 kHz, wavelength of 1047 nm, temporal pulse width of 5 – 15 ns, and single-pulse fluence of 6 – 17 J/cm^2. In order to characterize their impulse performance as a function of fluence, which should not depend on ablation material, an effective ablation spot area is defined as that obtained against aluminum, 1050A, as the reference material. An impulse that resulted from a single burst of 200 pulses is measured with the torsion-type impulse stand. Various impulse dependences on the fluence, which are not readily predicted from the optical properties of the material without ablation, are obtained. By fitting the experimentally measured impulse performance to Phipps and Sinko's model in the vapor regime, the effective absorption coefficient with laser ablation is evaluated, thereby resulting in three to six orders of magnitude larger than that without ablation. Among the polymers examined using polytetrafluoroethylene (PTFE) as the best volume absorbers, the highest momentum coupling coefficient of 66 μNs/J is obtained with an effective absorption coefficient more than six times smaller than that of the other polymers.

Lastly, in Chapter 5, concludes the present study by summarizing the contents in the previous Chapters.

Chapter 2.
Apparatus and methods

2.1 Experimental systems for impulse measurement

Figure 2.1 shows the schematic illustration of the experimental system. An ablator was mounted on one end of a torsion pendulum. The pendulum was placed in a vacuum chamber 0.7 m in diameter and 2.2 m in length. The vacuum chamber was evacuated to an ambient pressure of 2×10^{-2} Pa by a turbo molecular pump (2000 L/s, TMP-2003LM, Shimadzu co.) backed by a rotary pump (533 L/s, T2033SD, Alcatel). The output pulse from a laser was first sent into the vacuum chamber through a BK7 window and then focused by a 150 mm focal length achromatic lens onto the ablator. Laser ablation is occurred on the ablator surface, induce displacement of the torsion pendulum. The 18-μm-thick cellophane film was placed just behind the beam condensing lens with an oblique angle of incidence of 30° to avoid contaminating the lens against the exhaust ablation plume. The transmittance, T_i of the film corresponding to the 1047 nm pulse was measured to be almost 99 %. The incident angle to the ablator surface was 90 degrees with less than 5 degrees of allowance.

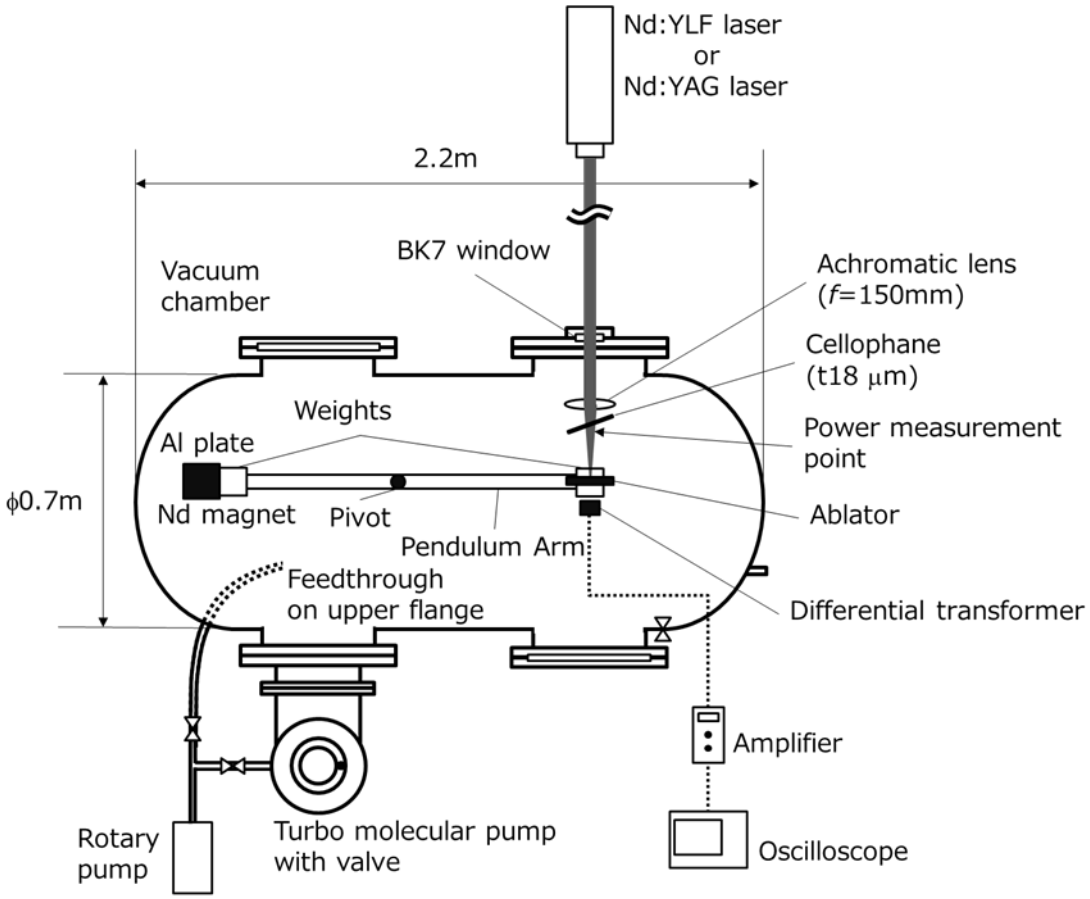

Figure 2.1 Experimental system.

2.1.1 Laser systems and operations

The specifications of the lasers, which were used in this study, are summarized in Table 2.1. The photographs are shown in Figure 2.2. Wavelength and pulsewidth of each laser are same order of magnitued. Nd:YLF laser can be used for investigating the performance under high pulse repetition frequency up to 10 kHz. While the pulse energy is small, fluence of 24 J/cm^2 is achieved by focusing. Nd:YAG laser can output relatively high energy pulse while the maximum repetition frequency is 1 Hz. Therefore, higher fluence and/or larger laser spot size are achieved. The larger spot size helps us to evaluate profile of burnt surfice.

Table 2.1 Laser specifications.

	Nd:YLF	Nd:YAG
Chapter	3,4	3
Manufacturer	Edgewave	QUANTA system
Wavelength, nm	1047	1064
Max. Pulse Energy, mJ	13	450
Pulsewidth, ns	5–15	7
Beam Diameter, mm	4	9
Max. Repetition Rate, Hz	10000	1

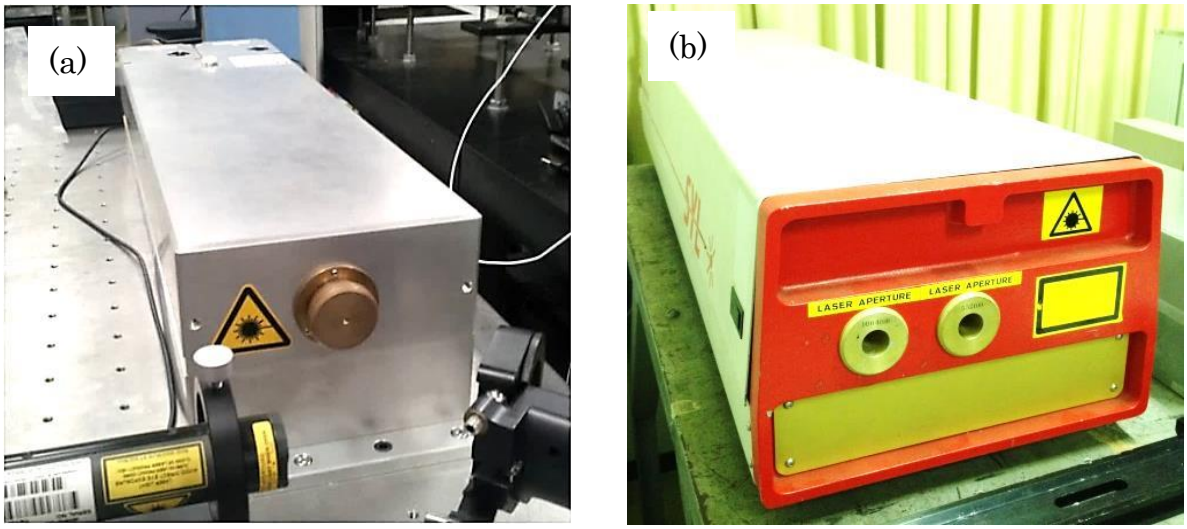

Figure 2.2 Photographs of laser, (a): Nd:YLF laser, (b): Nd:YAG laser.

The operation of Nd:YLF laser in burst mode as illustrated in Figure 2.3: A series of bursts could be output. A burst consists of N_b laser pulses with f; a single laser pulse has an energy of E_p. Total impulse generated by a burst of N_b pulses was measured with the torsion-type impulse stand which explained in detail in Section 2.1.3. The time interval between the bursts was set to 1.5 minutes. In preliminary experiment, in this range of interval, the effect of the interval on the impulse performance was confirmed to be negligible.

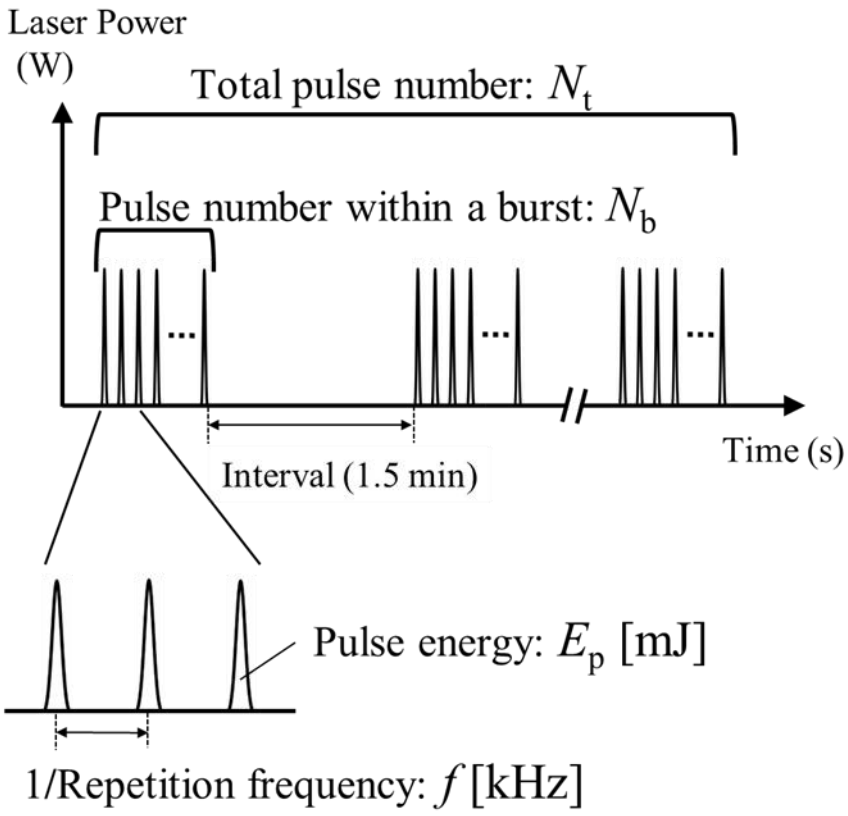

Figure 2.3 Specification of Nd:YLF laser pulse irradiations in burst mode.

The operation of Nd:YAG laser is illustrated in Figure 2.4. The measuring processes were as follows: the impulse generated by the first pulse was measured, then 23 laser shots were output with a certain time interval and the impulse generated by the 25th pulse was measured.

The process continued so impulses generated by pulse numbers of a multiple of 25 were obtained, until the impulse became too small to be measured by the torsion pendulum.

The time interval between pulses was set to longer than 10 s throughout this series of experiments. A preliminary experimental result indicated that the total impulse generated by repetitive pulse irradiation decreases with times intervals shorter than 10 s, while no significant difference was observed with time intervals longer than 10 s. One of the causes for this impulse degradation could be the temperature changing at the ablation area on the surface of the target. If the pulses are output at shorter interval times than the period that the target is sufficiently cooled, the temperature at the laser irradiating area will increase [32]. Higher surface temperature may enhance deepening of the crater and the impulse with the successive laser pulses may decrease quickly. The relationship between crater deepening and impulse will be discussed in the Section 3.3.

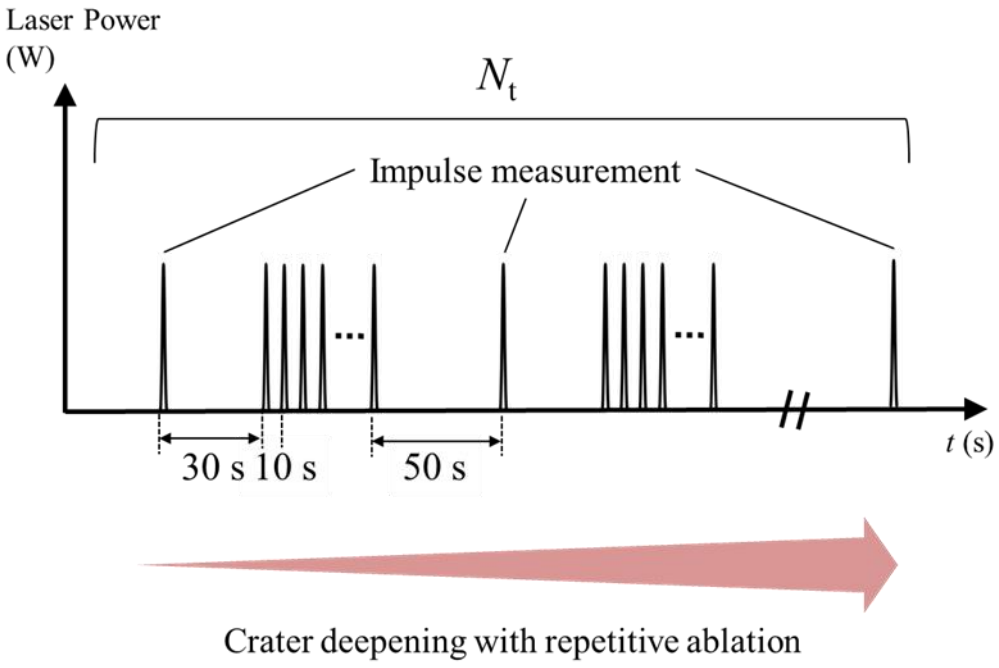

Figure 2.4 Specification of Nd:YAG laser pulse irradiations.

2.1.2 Vacuum facilities

Space chamber has the volume of 0.7 m diameter and 2.2 m long. Figure 2.5 shows the picture of the chamber. The vacuum chamber is made of stainless steel and evacuated to a pressure of 2×10^{-2} Pa by a turbo-molecular pump (2000 L/s, TMP-2003LM, Shinadzu co.) backed by a rotary pump (533 L/s, T2033SD, Alcatel). The pressure is measured using a Pirani gauge (0.4 – 2.7 × 10^{3} Pa, GP-1S, ULVAC) and an ionization gauge (10^{-7} – 3.8 × 10^{-1} Pa, ANELVA, MIG-061). The chamber is used for the experiment in Chapter 3 and Chapter 4.

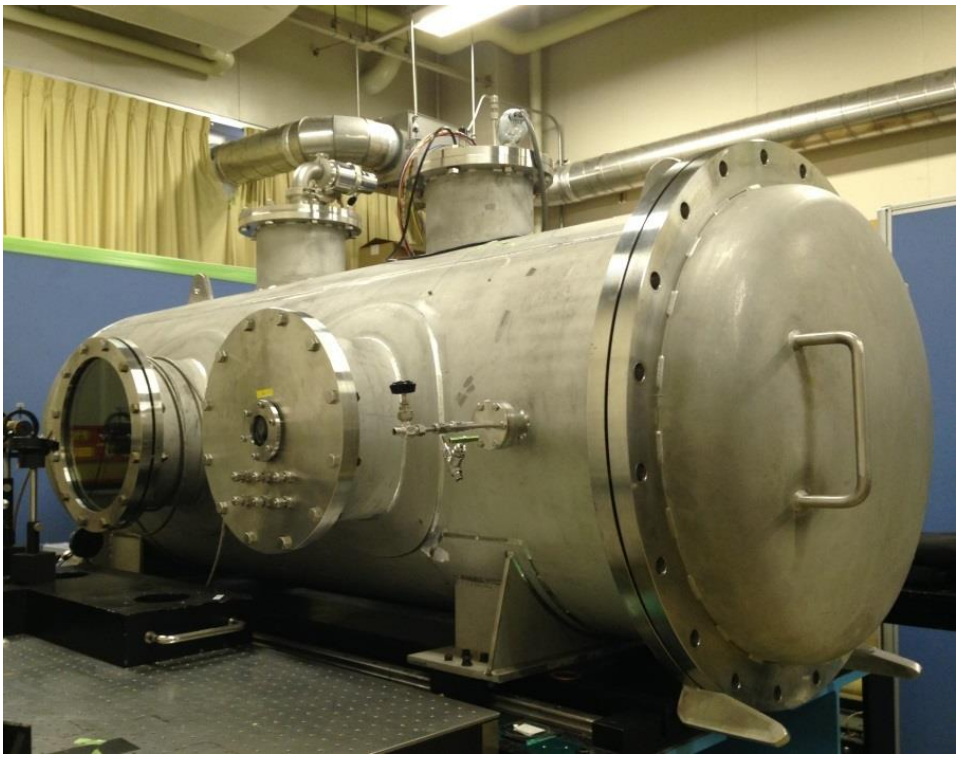

Figure 2.5 Space chamber.

2.1.3 Impulse measurement

2.1.3.1 Principle and method

The maximum displacement of the pendulum arm is proportional to the imparted impulse. An impulse that is induced by a single laser pulse can be modeled using the Dirac delta function. [36] The equation of motion of the balance yields

$$J\frac{\mathrm{d}^2\theta}{\mathrm{d}t^2}+C\frac{\mathrm{d}\theta}{\mathrm{d}t}+K\theta=r_L\sum_{i=1}^{N_t}I_{m,i}\delta\left(t-(i-1)\Delta\tau_L\right) \qquad 2.1$$

where J, C, and K are the angular momentum of inertia, damping coefficient, and restoring force, respectively. r_L, N_t, $I_{\mathrm{m},i}$, and $\Delta\tau_\mathrm{L}$ are the radial location of the laser pulse irradiation, total number of laser pulses, impulse induced by the ith laser pulse, and time interval between successive laser pulses. $\theta << 1°$ is assumed. The maximum deflection is decreased from the ideal value by increasing the temporal impulse duration, i.e., the measurement error is increased. Suzuki et al. [36] estimated the measurement error as shown in Figure 2.6. g_e is the ratio of the maximum deflection angle induced by the N_t-impulse exertions with a constant time interval of $\Delta\tau_\mathrm{L}$ to the maximum deflection angle when the same impulse is induced instantaneously. The horizontal of Figure 2.6 is the dimensionless temporal impulse duration with repetitive irradiation, which is divided by the natural oscillation period of the pendulum, τ_0. The temporal deflection signal could be fitted to a damped oscillation expression:

$$B=A\sin\left(\omega(t-t_0)\right)\exp\left(-C(t-t_0)\right) \qquad 2.2$$

A typical pendulum oscillation signal is shown in Figure 2.7. By fitting the temporal deflection of the pendulum arm with Eq. 2.2, the amplitude, A, was obtained.

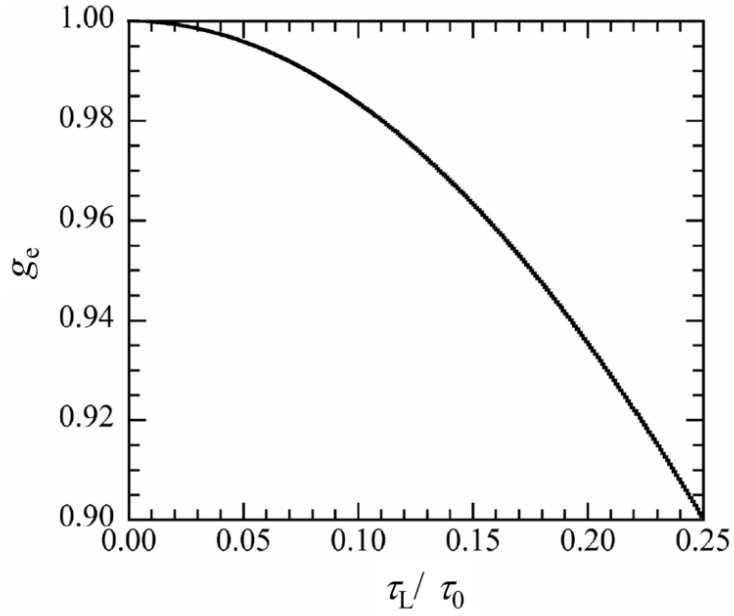

Figure 2.6 Decrement of pendulum gain with increasing τ_L.

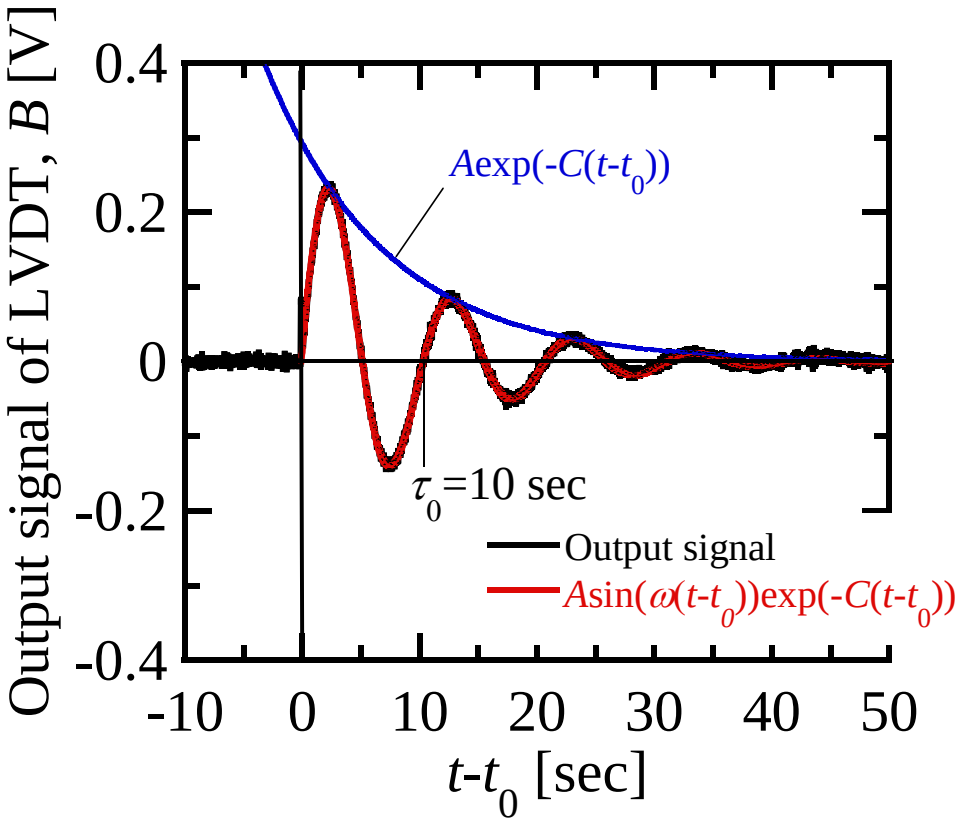

Figure 2.7 Example of an oscillation signal of the torsion pendulum, E_p = 8.0 mJ, $N_b = N_t$ = 200, f = 1 kHz (burst duration; 0.2 s).

2.1.3.2 Torsion type impulse stand

Figure 2.8 shows the image of a torsion-type balance [36] that has a 1-m-long, horizontally set, main arm made of aluminum. The arm is supported by two torsion springs on the upper and lower surfaces at the center of the arm. The impulse of the interest is the time integration of the reaction force. With laser pulse irradiations, the laser-ablated jet was ejected perpendicularly to the ablator surface, which induced the oscillation of the torsion pendulum arm. The temporal deflection of the arm was measured using a linear variable differential transformer (resolution; 0.29 V/mm, Model 1591ST, Shinko Electric co.) and recorded by a digital oscilloscope. The impulse range applicable to the pendulum could be controlled by adjusting the mass of the counterweights which were mounted each end of the pendulum arm or by changing the spring constant of the torsion springs. In this research, in order to measure an ablation impulse in the 1 to 100 μNs range, the mass of each counter weight set to 1 kg and the torsion springs which the spring constant is 0.0958 Nm/rad is used. By this arrangement, its natural oscillation period, τ_o was about 10 seconds. Based on [36], the error in the impulse measurement due to a deflection of the pendulum arm in the period of a burst of up to 1 second was estimated to be less than 2 %. An eddy current damper was used to keep a reasonable oscillation turnaround. The ratio of I_m to A was calibrated using an impact hammer (18.7 mV/N, 086E80, PCB Piezotronics) as shown in Figure 2.9.

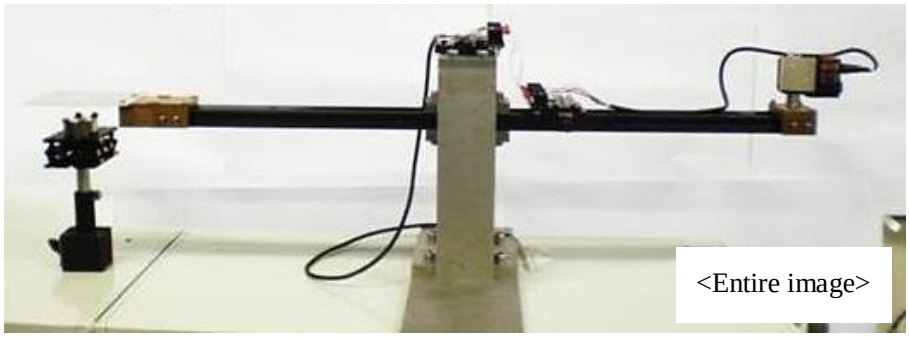

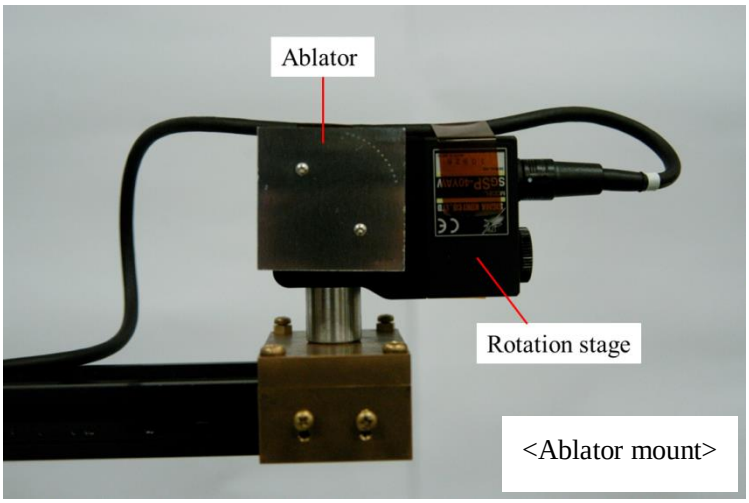

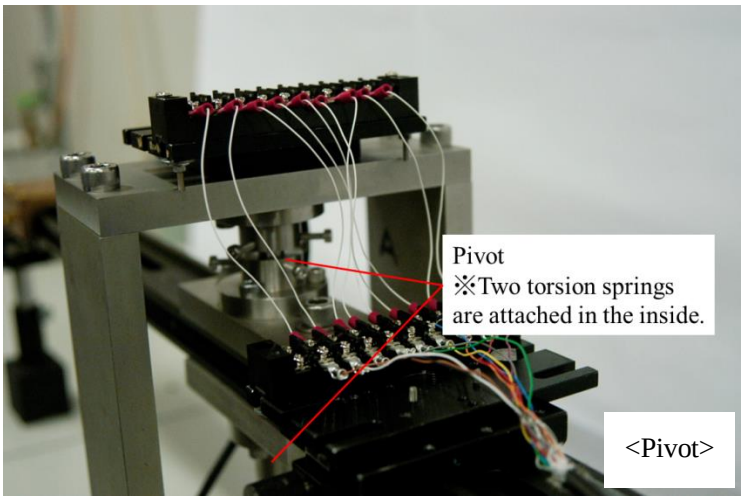

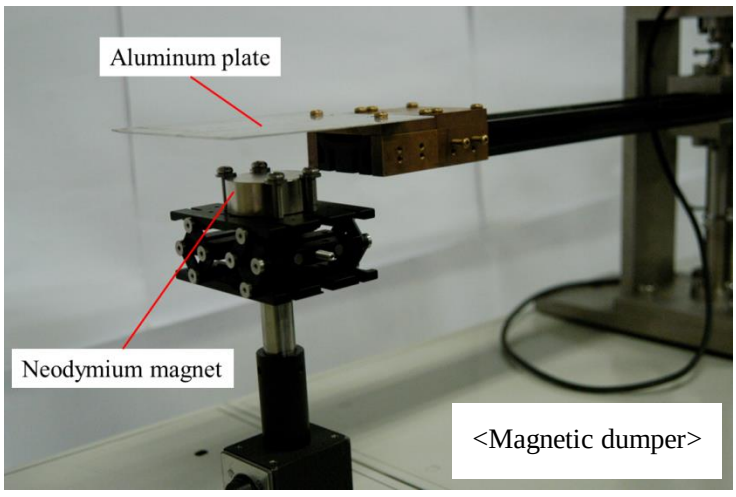

Figure 2.8　Image of the torsion type impulse stand.

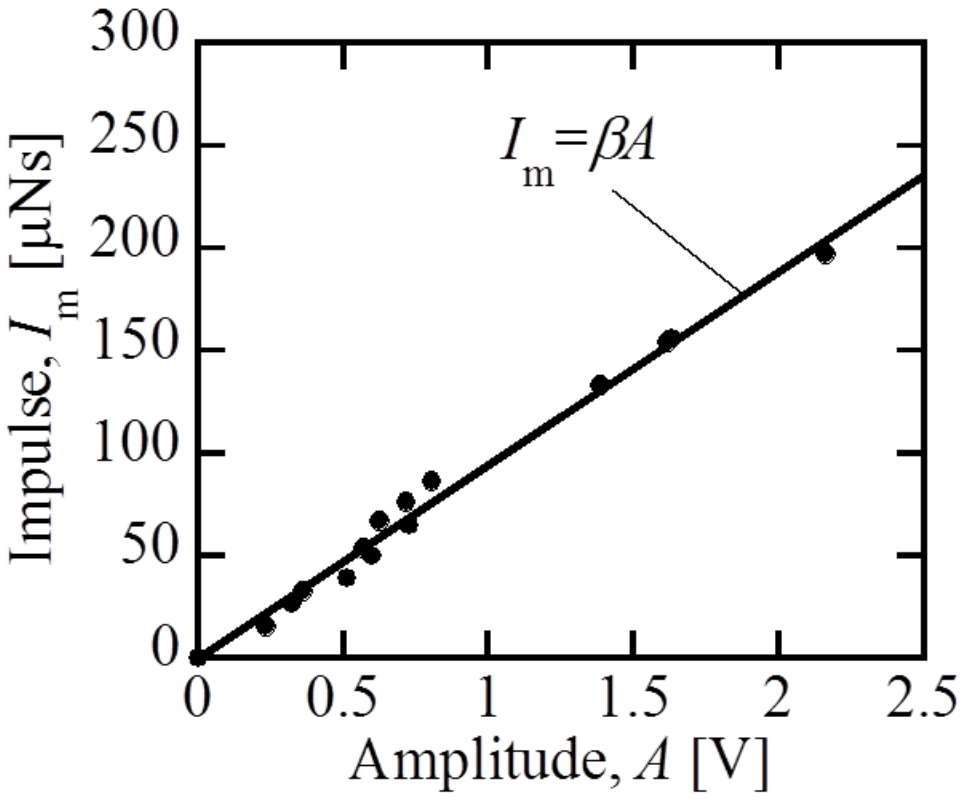

Figure 2.9 Example of torsion type pendulum calibration. A linear fit of an impulse, I_m, to pendulum oscillation amplitude, A, was obtained in the I_m range from 15 μN-s to 197 μN-s, β = 94 μN-s/V.

2.2 Evaluation of ablation spot area

The ablation spot area, S, is evaluated through measurements using a confocal laser scanning microscope (horizontal resolution 0.01 μm, height resolution 0.01μm, VK-9500, KEYENCE Company). While this device has functions to measure three-dimensional shapes, just a two-dimensional image of the ablator surface is used for evaluating S. The area of the burn pattern generated because of ablation on the ablator is measured using analysis software. An example of the measurement is displayed in Figure 2.10. The edge of the dark region is traced manually. S is the area surrounded by the trace line. Although the depth of the region was not measured in the present study, the ablated region is darker than the surrounding regions. Ideally,

the area is the region at which the laser intensity is above the ablation threshold. However, the actual dark area of several materials is expanded because of heat conduction from the ablated region and radiation from the ablation plume. The degree of expansion depends on the material properties. In this study, aluminum is used for evaluating the ablation area, because of the area stability against the variation of N_t and E_p. The moderate stability of aluminum is explained in detail in Section 4.1.

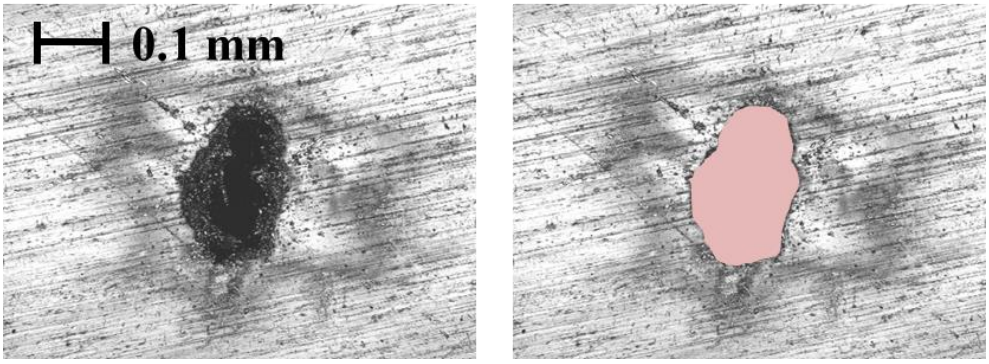

Figure 2.10 Example of ablation spot area measurement, Aluminum, E_p = 5.03 mJ, N_b = 1000.

2.3 Ablated mass measurement

The ablated mass is measured with an electronic balance (resolution of 0.1 mg, AW320, Shimadzu Company). The measurement is repeated five times in each ablator and the averaged value is used.

Figure 2.11 Image of the electronic balance.

2.4 Characteristic parameters

2.4.1 Control parameters

The influence of the fundamental laser parameters such as fluence, wavelength, and pulse-width have been investigated and discussed. Representative reports are introduced briefly.

The impulse mainly depends on the incident laser fluence, ϕ_p, which is the ratio of the laser pulse energy to the focal spot area. It is known from the experimental result that C_m increases from zero to the maximum value and then decreases with increasing ϕ_p [9]. Phipps et al. [29] proposed a model to relate C_m and $\phi_p \lambda \tau^{-1/2}$ during the plasma regime based on existing data and theory, where ϕ_p, λ, and τ are fluence, wavelength, and pulse width, respectively. The author concluded that after attaining maximum value, C_m decreases with increasing $\phi_p \lambda \tau^{-1/2}$, because "plasma shielding" becomes gradually dominant. Plasma shielding is re-radiation or scattering of the incidence beam by plasma near the ablator surface. Phipps et al. [46] also proposed a C_m model of

volume absorber during vapor regime. Sinko and Phipps, in 2009, [40] combined these models as they describe, in a continuous way, the transition effects from the onset of vaporization to the plasma regime.

With increasing ϕ_p, first, the ablator evaporation contributes to the impulse and then the discharging rate starts increasing. At this stage, the laser energy is absorbed by the plasma electrons. This is also called inverse bremsstrahlung. The ratio of the absorption process increases with increasing wavelength [51,52].

The pulse width range of the existing laser is from femtosecond to millisecond. In general, the larger the pulse energy, the wider is the pulse width. For ultrafast pulses, the energy is deposited over a timescale, which allows most of the energy to interact with the surface because the timescale of plasma formation is few picoseconds. Because of this feature, the ultrafast pulse avoids the C_m decrement caused by plasma shielding. However, the pulse energy of the ultrafast pulse is quite small in the current technology; the impulse is insufficient for practical use. On the other hand, for a pulse width of nanosecond or longer, plasma is generated before all the laser pulse energy can reach the surface and partially shields the energy of the incoming beam. Based on a different selection of the published data, Phipps et al. [9,11] reported that the intensity required to reach the plasma-ignition temperature on a surface varies such that $I\tau^{1/2}$ is constant, 4.79×10^8 $Wm^{-2}s^{1/2}$ at beyond 100 picosecond of τ. This means that C_m takes the maximum value at the constant because plasma decreases C_m by plasma cutoff. Temporal impulse duration induced by a single pulse with τ should be beyond τ because the ablation force is continue to affecting on the ablator surface after end of the laser pulse. Anju et al. [57] investigated how temporal pressure history acts on the ablator, due to laser ablation with VISER (Velocity Interferometer System for any Reflector) measurement. As a result, the pressure duration of aluminium against the Nd:YAG laser with a temporal pulse width of 7 ns (FWHM) and a wavelength of 1064 nm was about 50 ns, whereas it was about 2 μs with POM against TEA CO_2

laser with a temporal pulse width of 140 ns (FWHM) and a wavelength of 10600 nm.

The control parameters of this study are introduced as follows.

This study treats pulse repetitive irradiation. Therefore, the total number of laser pulses, N_t, and laser pulse repetition frequency, f, are controllable parameters. In particular, the number of pulses within a burst is defined as N_b, when operated with burst irradiation by the Nd:YLF laser. The total laser energy, $E_t = E_p \times N_t$ is also a controllable parameter.

The ablator material is a main parameter in Chapter. 4. Aluminium (1050A) is used as a metal. POM and PTFE are milky-white crystalline polymers, while PMMA, PC, and PET are transparent amorphous polymers.

2.4.2 Performance parameters

The momentum coupling coefficient, C_m, is defined as the ratio of impulse, I_m, to the incident energy of a single laser pulse, E_p (or as the ratio of pressure, p, to the radiation intensity, I, for a continuous-wave laser).

$$C_m = \frac{I_m}{E_p}\left[\text{N-sec/J}\right] = \frac{p}{I}\left[\text{N/W}\right] \tag{2.3}$$

The specific impulse is described by

$$I_{sp} = \frac{v_e}{g}\left[\text{sec}\right] \tag{2.4}$$

where, v_e and g are the average exhaust velocity of the ablated material and gravitational acceleration, respectively. Ablation energy efficiency, η, which is the ratio of kinetic energy to E_p is as follows.

$$\eta = \frac{mv_e^2}{2E_p} = \frac{g}{2} C_m I_{sp} \tag{2.5}$$

In the case of constant η, C_m, and I_{sp} are inversely proportional to each other. Therefore, it is important to consider the balance of C_m and I_{sp}. I_{sp} should be preceded for space transportation because the fuel consumption must be suppressed for transport to a faraway destination such as Mars. On the other hand, C_m should be preceded for space debris deorbiting, altitude modification of the satellite, and so on. This is because the fuel consumption is not so important for these applications and an increment of C_m benefits cost reduction by miniaturization of the laser device or by a larger momentum with the same amount of E_p.

Chapter 3.
Impulse characteristics of aluminum

The purpose of this Chapter is to investigate the laser ablation impulse performance induced by repetitive pulse irradiation as well as accompanying phenomena.

Firstly, impulse characteristics against high frequency (0.3 – 8.0 kHz) repetitive Nd:YLF laser (wavelength of 1047 nm, pulse duration of 5 – 15 ns) pulses onto an aluminum ablator in a vacuum environment is discussed. The laser is operated in burst modes with a varying pulse repetition frequency, and single pulse energy and number. The fluence range is from 6 – 24 J/cm^2. The burst is repeated until the impulse is saturated. A torsion pendulum is used to measure the total impulse generated in a single burst. The accuracy is better than 2 % even with a burst period of 1 s. The influence of the pulse repetition frequency, total laser pulse energy, and fluence are clarified. Propulsion performance is reported through the exhaust mass measurement. The influence of the fundamental parameters such as the pulse repetition frequency, single pulse energy, and pulse number of the induced impulse under a high pulse repetition frequency (0.3 – 8.0 kHz) is revealed. The impulse decreases with increasing pulse number within the fluence range of 6 – 24 J/cm^2. While the formation and deepening of the crater accompanied by repetitive ablation clearly affects the impulse characteristics, the crater with a diameter in the order of 100 μm is somewhat small for observation.

Subsequently, impulse characteristics of larger energy pulses of the Nd:YAG laser (wavelength of 1064 nm, pulse duration of 7 ns) are investigated. The pulse repetition frequency of this experiment (< 0.1 Hz) is much lower than that of the Nd:YLF laser. A larger fluence

range of 16–75 J/cm^2 is achieved. Larger crater formed on the ablator is helpful for investigating the relationship between impulse and the crater profile. The changes in surface area caused by crater deepening are measured with a laser microscope, and then are used for calculating the effective fluence. The fluence is compared to a corresponding variation in the momentum-coupling coefficient with repetitive pulses. Through discussion, the influence of the effective fluence will be revealed. The wall confinement effect on the impulse is not observed. Even then, further discussion is avoided because other factors such as oblique incidence, directionality of the ablation impulse on the inner wall of the crater, and re-solidification of the molten Al ejected from the bottom region near the entrance of the crater, may all affect the impulse.

3.1 Impulse characteristics with small energy pulses

3.1.1 Effect of laser pulse repetition frequency in burst irradiation

The dependence of I_m on laser pulse repetition frequency, f, with a constant E_p induced in a single burst, $N_b = N_t = 200$, is shown in Figure 3.1. The data scattering is conceivably attributed to the modest reproducibility of the single pulse energy in the repetitive frequency range $f < 1.0$ kHz. Yet, with ϕ_p =11 J/cm^2, I_m shows a slightly-decreasing trend as f increases.

It is predictable that if f becomes too high, the interaction between ablation generated plume with succeeding pulses, including cutting off the laser beam against the ablator surface, would appear. However, according to Ref. [14], the plume disperses in only a few micro seconds. In this study, the pulse-to-pulse interval in a burst, $1/f$, was 125 μs (for f = 8 kHz) at a minimum. This somehow explains the insensitivity of I_m to f shown in the present experiments.

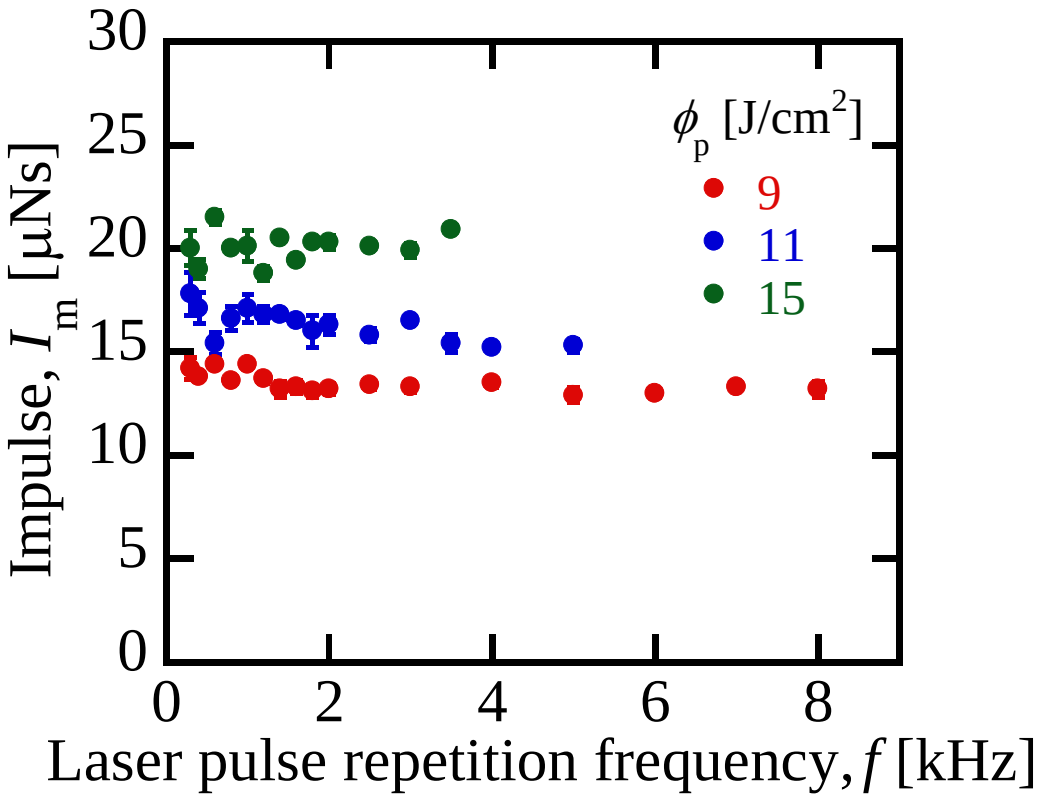

Figure 3.1 Impulse dependence on f, $N_t = N_b = 200$, average of 3 runs in each operation condition, the length of an error bar corresponds to a standard deviation.

3.1.2 Integrated impulse performance

As was mentioned in Section 2.1.3, the necessary condition for the error in the impulse measurement to be smaller than 2 % is $N_b/f < 1$. This implies that with f = 1 kHz, N_b should be smaller than 1000. Moreover, I_m may depend on the distribution and history of the target temperature near the laser spot, which are influenced by N_b. Therefore the dependence of I_m on N_b needs to be investigated. In this study, I_m was measured with N_b = 100, 500 and 1000. Figure 3.2 shows a typical I_m dependency on N_t. In case of N_b = 100, a series of burst operations were done as long as the impulse increment was sufficient to keep reasonable accuracy. Then, N_b was increased to 200 to improve the signal-to-noise ratio.

With constant f and ϕ_p, I_m could be well fitted to a single function of N_t irrespective to the value of N_b. With ϕ_p = 21 J/cm^2, the largest difference appears at N_t = 1000, a 4 % decrement from

the average performance. The result shows that, under the experimental condition studied, N_b has insignificant influence on the impulse performance. Moreover, Figure 3.2 shows the possibility that higher ϕ_p leads to higher saturation of I_m. So ϕ_p is varied into smaller steps in the following experiment.

Figure 3.3 plots I_m dependence on the total laser energy E_t. Impulse generation is significantly influenced by ϕ_p. I_m increased and reached saturation with increasing E_t. The saturation value of I_m increased with increasing ϕ_p. Figure 3.4 shows an example of cross-sectional profile of a crater generated by laser pulses with the specified irradiation conditions. In this case, a crater with a diameter of 180 μm and a depth of 300 μm at its bottom is formed. Around the crater, a rim with a width of 80 μm and an average height of 100 μm is formed by ejected mass from the crater. With this shape, the effective incident angle of laser pulse on the ablator surface is increased from the initial value of 0. The saturation of the overall impulse could be explained as follows. It is well known that C_m is a function of the fluence ϕ_p. There is a threshold fluence in which C_m vanishes (no occurrence of ablation) when ϕ_p is smaller than the threshold. With more irradiation pulses, a crater is formed and its aspect ratio becomes larger. Figure 3.4 shows an example of the crater profile. As illustrate in Figure 3.5, assuming the laser beam cross-sectional area is fixed within the depth duration of the crater, the effective irradiated area at the crater inner wall becomes larger. Therefore, the ϕ_p on the crater inner wall will decrease with increasing pulse number N_t. As a result, saturation of the overall impulse appears when ϕ_p is lower than the laser-ablation threshold. This result indicates that, in practical applications, avoiding generating a deep crater is important for repetitive pulsed laser ablation.

Dividing I_m generated with 100 pulses by the corresponding laser energy, C_m was evaluated as a function of E_t (Figure 3.6). The smaller the ϕ_p, the more rapidly C_m decreases with increasing E_t. In this study, the C_m with a single laser pulse is too small to be measured directly with the torsion pendulum. However, C_m with a single laser pulse can be obtained as the vertical axis

intercept of the fitted curves of C_m in Figure 3.6. As shown in Figure 3.7, these values are comparable to those obtained from single-pulse shots by D'Souza [31] using a Nd:YAG laser (1064 nm wavelength).

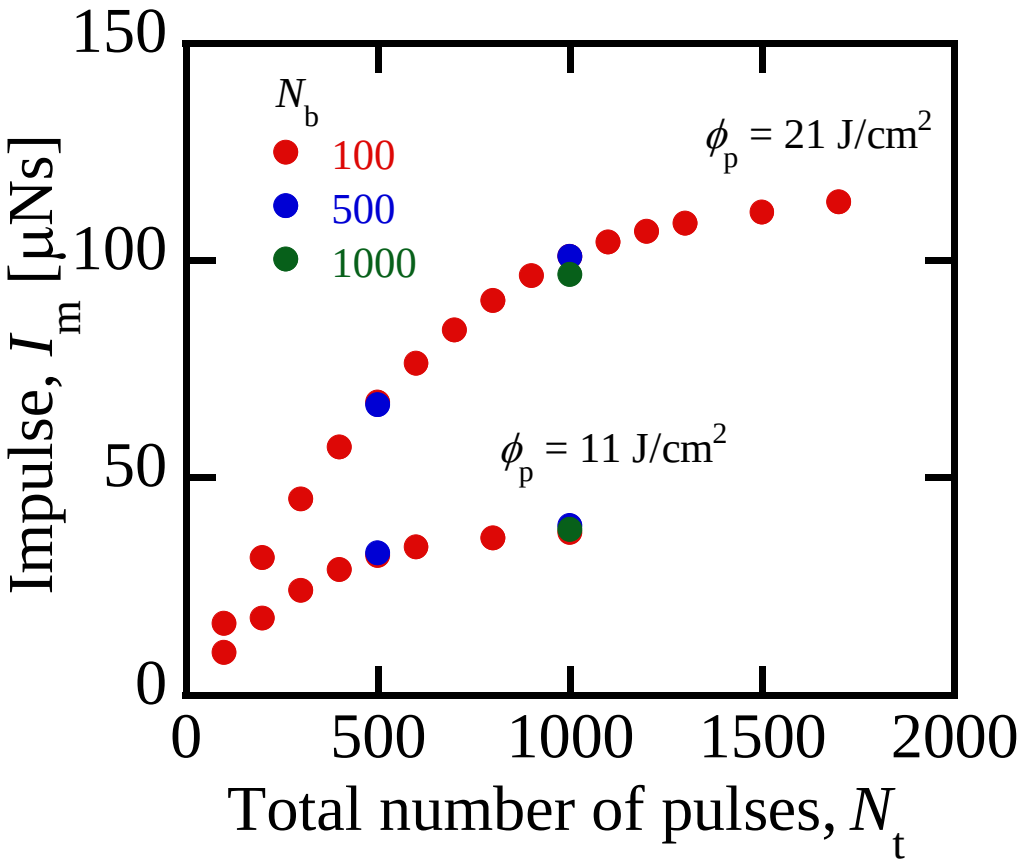

Figure 3.2 Impulse dependence on N_t for various N_b, f = 1 kHz, laser spot area is 5.2×10^{-8} m^2, average in 3 runs in each condition, N_b = 100 - 200 (red symbols), N_b = 500 (blue symbols), N_b = 1000 (green symbols).

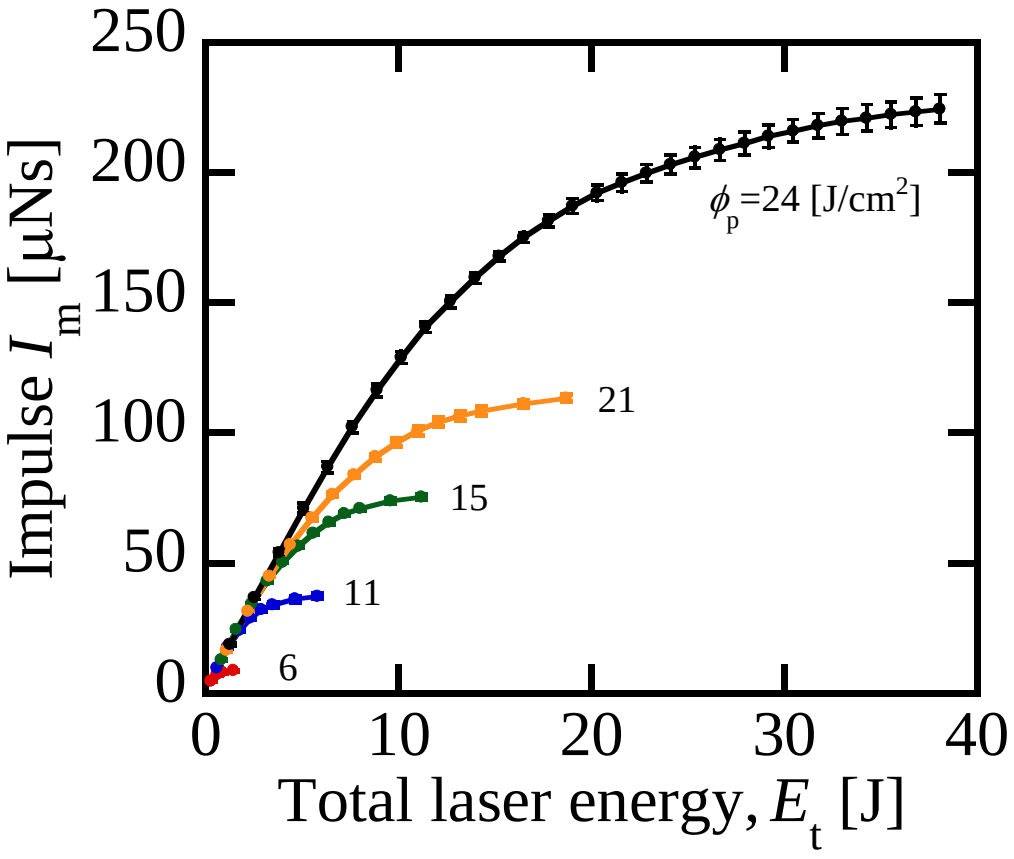

Figure 3.3 I_m vs. E_t, f = 1 kHz, N_b = 100 (200 in a few bursts), average of 3 runs each, error bars correspond to the standard deviation the data set.

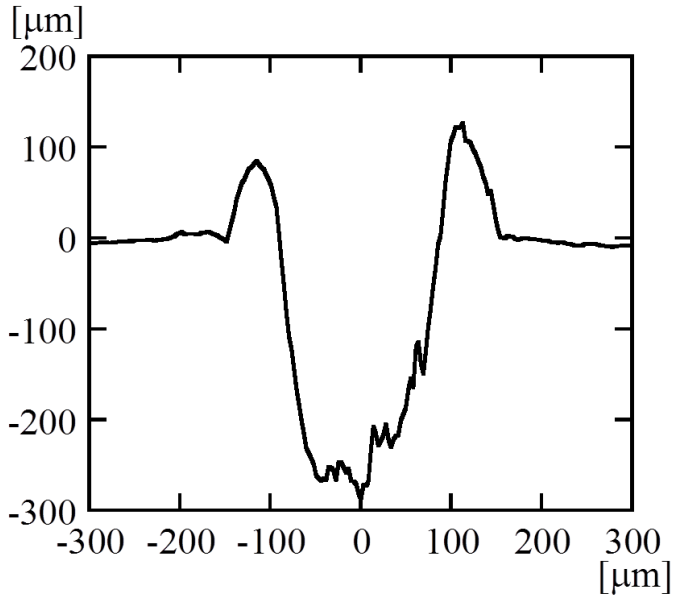

Figure 3.4 Example of cross-section of crater profile, f = 1 kHz N_t = N_b = 100, ϕ_p = 15 J/cm^2

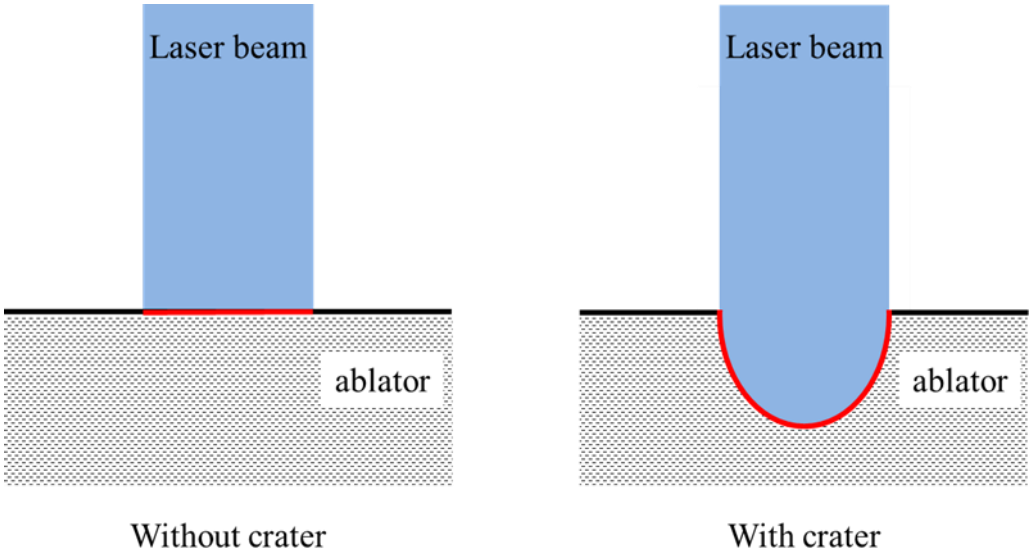

Figure 3.5 Enlargement of the exposed area caused by the crater formation.

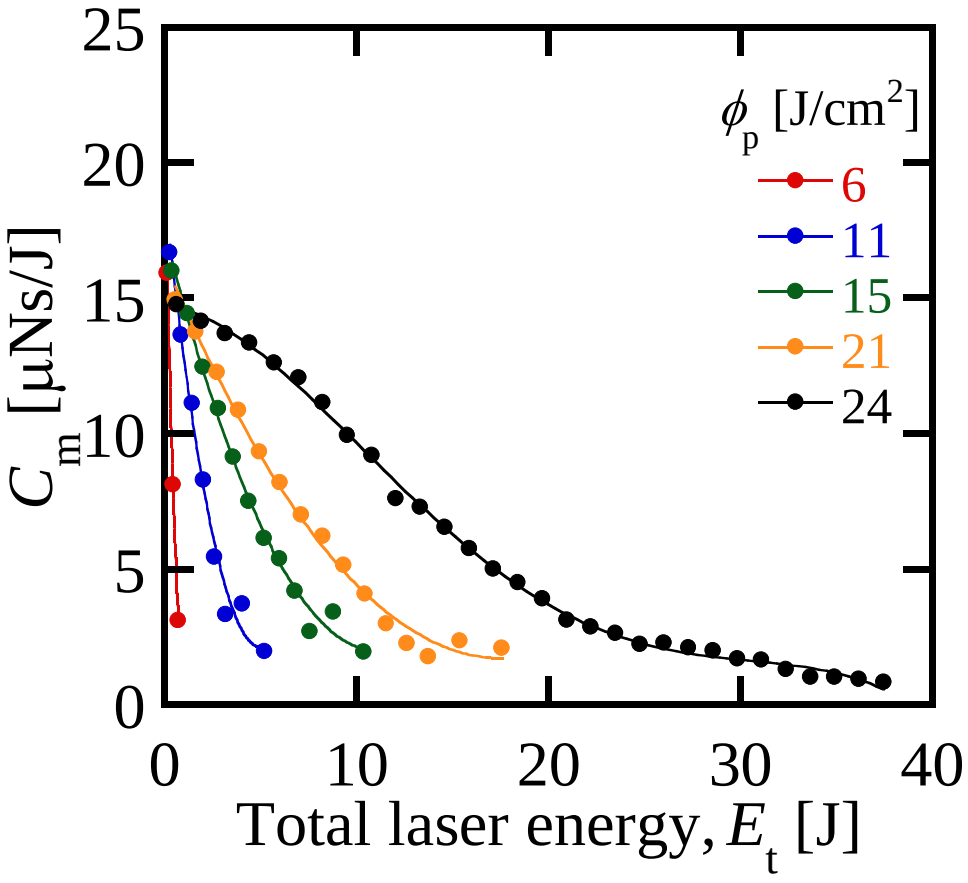

Figure 3.6 Momentum coupling coefficient C_m as a function of total energy E_t , f = 1 kHz.

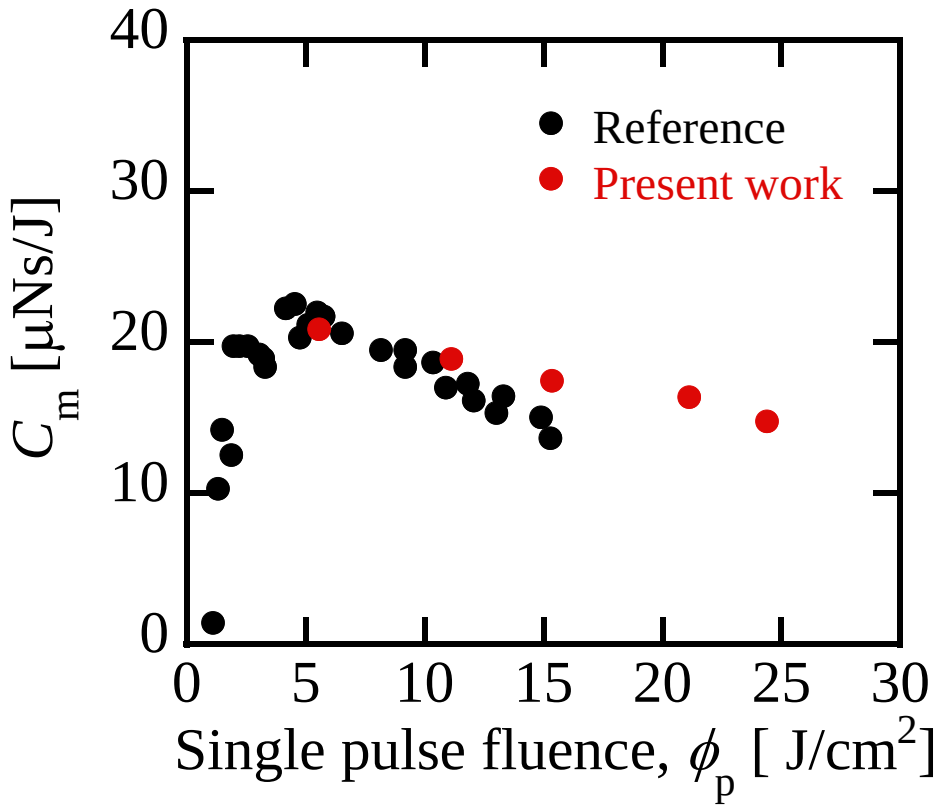

Figure 3.7 Verification of C_m vs. ϕ_p with the single pulse. In Ref. [31], the data was obtained under vacuum by ablating an aluminum target with a Nd:YAG laser which has a 5 ns pulse width.

3.1.3 Averaged exhaust velocity

To estimate the exhaust velocity of the ablation ejected material, the impulse and ablated mass must be measured [14]. Unfortunately, the crater generated by repetitive irradiation at the surface of the ablator had a rim with a density different from the virgin ablator. Therefore, the mass estimated from the crater profile was not accurate [53]. The ablated mass in a single laser pulse or burst was too small to be directly measured with an electronic balance (resolution of 0.1 mg, AW320, Shimadzu Company). Therefore, the ablated mass was evaluated after many pulses as follows: After a single burst irradiation of N_t laser pulses, the ablator was rotated by 2.5 deg around its surface normal, and another burst with the same N_t was irradiated on the virgin ablator surface. This process was repeated until the total rotation angle was 360 deg. Then, the target was

slid a certain distance so that the radius of rotation was different from the previous one. In this way, the formation of a new circle of ablation spots was repeated until the total ablated mass became sufficiently large to be measured by the balance. The typical ablator plate after the experiment shown in Figure 3.8. Each mark on the ablator plate is formed by a single burst. The average ablated mass in a single burst $m(N_b)$ was evaluated as the total ablated mass divided by the total burst number (Table 3.1).

The average exhaust velocity $\bar{v}$, the corresponding ablation efficiency $\bar{\eta}$ [54], and the corresponding C_m from 0 to 500 pulses and from 500 to 1000 pulses are calculated by the following equations:

$$\bar{N}_t(N_{t,1}, N_{t,2}) = (N_{t,2} - N_{t,1})/2 + N_{t,1} \tag{3.1}$$

$$\bar{C}_m(N_{t,1}, N_{t,2}) = (I_m(N_{t,2}) - I_m(N_{t,1}))/(E_t(N_{t,2}) - E_t(N_{t,1})) \tag{3.2}$$

$$\bar{v}(N_{t,1}, N_{t,2}) = (I(N_{t,2}) - I(N_{t,1}))/(m(N_{t,2}) - m(N_{t,1})) \tag{3.3}$$

$$\bar{\eta}(N_{t,1}, N_{t,2}) = \psi \frac{(m(N_{t,2}) - m(N_{t,1}))\bar{v}^2(N_{t,1}, N_{t,2})}{2(E_t(N_{t,2}) - E_t(N_{t,1}))} \tag{3.4}$$

where ψ is the ratio of one-dimensional kinetic energy with thermal contribution to that without it, and it is assumed to be unity.

As indicated in Table 3.2, with increasing N_t, the propulsion performance is worse: $\bar{C}_m$ and $\bar{v}$ decrease from 12 – 4 μN-s/J and from 11.2 to 6.5 km/s, respectively. The calculated $\bar{\eta}$

decreased from 0.077 to 0.033 when $\overline{N_t}$ changed from 250 to 750.

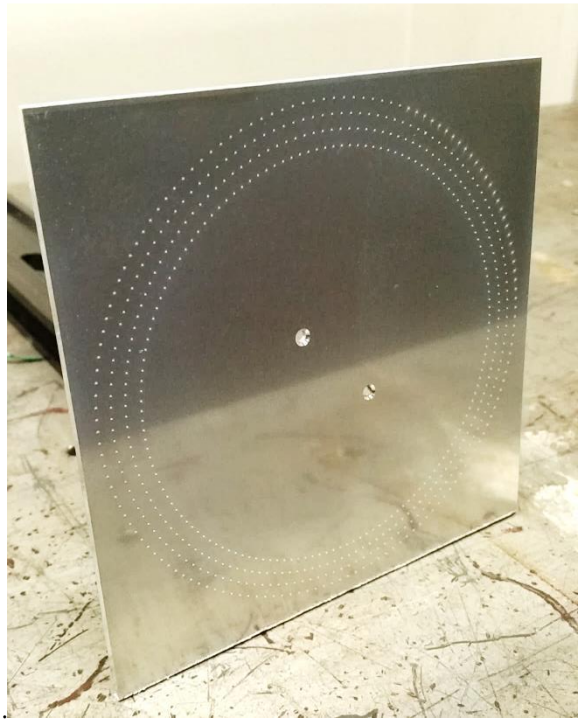

Figure 3.8 Image of an ablator plate after 432 bursts, 150 mm×150 mm×5 mm.

Table 3.1 Ejected mass and impulse generated over N_t pulses in a burst, average of 432 bursts, ϕ_p = 24 J/cm^2, f = 1 kHz.

N_t		500	1000
m	[μg]	7.7	17.4
I_m	[μNs]	87	150

Table 3.2 Average impulse performance, ϕ_p = 24 J/cm^2, f = 1 kHz.

$N_{t,1}$		0	500
$N_{t,2}$		500	1000
$\bar{N}_t(N_{t,1}, N_{t,2})$		250	750
$\bar{C}_m(N_{t,1}, N_{t,2})$	[μN-s/J]	12	4
$\bar{v}(N_{t,1}, N_{t,2})$	[km/s]	11.2	6.5
$\bar{\eta}(N_{t,1}, N_{t,2})$		0.077	0.033

3.2 Impulse characteristics with large energy pulses

The experimental setup for impulse measurement in this work was almost identical to that explained in the Section 2.1. The laser used here is a Nd:YAG laser (wavelength 1064 nm and pulsewidth 7 ns). The laser pulse was irradiated onto the ablator with normal incidence. The ablation spot area, S, was set to 4.5×10^5 μm^2 for all experimental conditions. The single-pulse fluence, ϕ_p, can be expressed as below.

$$\phi_p = \frac{E_p}{S} \tag{3.5}$$

For varying ϕ_p, the energy of a single laser pulse, E_p, was changed from 70 mJ to 330 mJ keeping S constant, 4.5×10^5 μm^2. Therefore, ϕ_p was changed from 16 J/cm^2 to 75 J/cm^2. For studying the effects of crater formation on the impulse, only the impulse after selected pulse numbers were measured.

Figure 3.9 shows C_m dependence on the total laser energy, E_t, with repetitive irradiation. Each plot is obtained as the averages of four tests under each operating conditions, the error bar

represents the standard deviation for each group of data sets. The large standard deviation of the smallest ϕ_p is caused by the performance of the laser, which has larger scattering with smaller E_p. For the case of ϕ_p = 16 J/cm^2, C_m simply decreases as E_t increases. With a ϕ_p of 25 and 29 J/cm^2, C_m does not decrease immediately. In the case of a ϕ_p of 45 and 75 J/cm^2, C_m increases once with increasing E_t, and then decreases. The highest total impulse with repetitive irradiation, $I_{m\ t} = \int C_m dE_t$, is obtained in the case of ϕ_p of 45 J/cm^2. These tendencies are discussed further in the following section. In addition, the C_m with the first pulse gradually decreased as ϕ_p increases. This tendency is the same as a result shown in Figure 3.7 in the Section 3.1.2. We consider that this is because of re-radiation or scattering of the incident laser pulse by high-density plasma near the ablator surface [29].

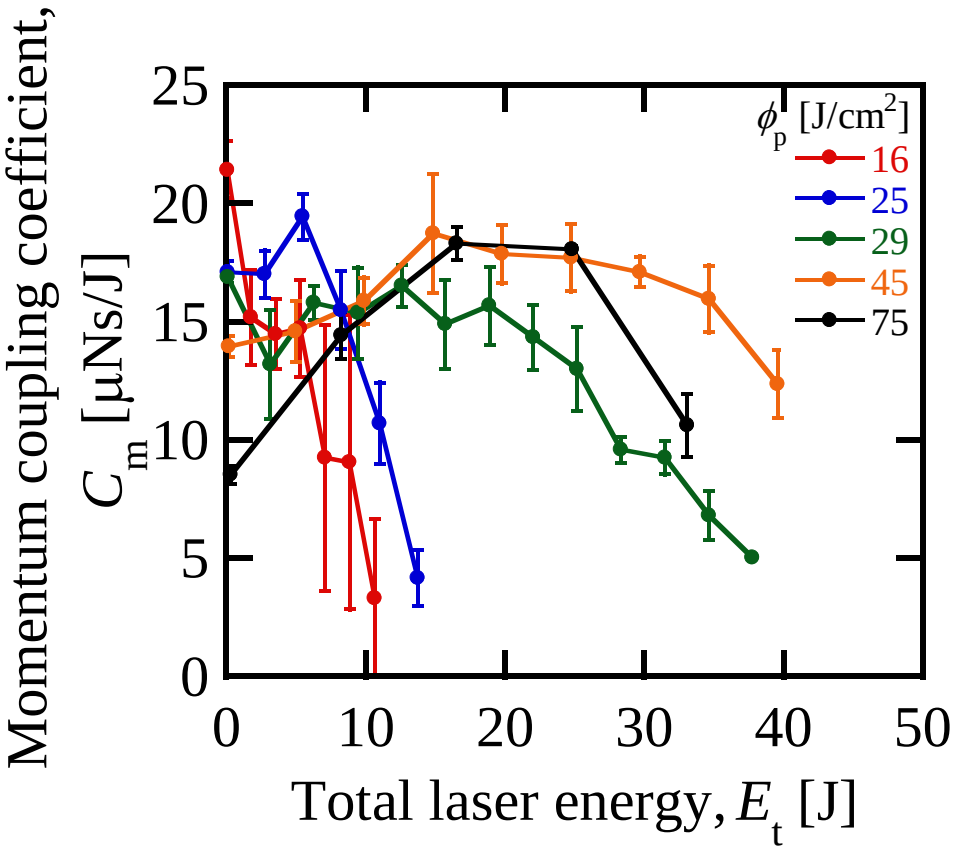

Figure 3.9 C_m dependence on E_t, Nd:YAG laser, λ = 1064 nm, τ = 7 ns, f < 0.1 Hz, laser spot area is 4.5×10^5 m^2, average in 4 runs in each condition.

The C_m characteristics, which continuously change with ϕ_p, are consistent with those obtained using the Nd:YLF laser, as shown in Figure 3.6. While the laser is different, the experiment with the Nd:YLF laser covers a low range of ϕ_p, 6 – 24 J/cm^2; the Nd:YAG laser covers high range of ϕ_p, 16 – 75 J/cm^2. ϕ_p in the range 16 – 24 J/cm^2 is covered in both experiments. In Figure 3.6, the slope of C_m decreases with increasing ϕ_p. The inflection point appears at E_p = 5 J with ϕ_p = 24 J/cm^2. Similarly, in Figure 3.9, C_m does not decrease immediately at a ϕ_p of 25 J/cm^2, while C_m sharply decreases at a ϕ_p of 16 J/cm^2. C_m in both experiments is not identical even at similar ϕ_p values because several conditions such as the energy profile, spot size, and pulse repetition frequency are different. Based on this consistent observation in each experiment, the same factor may dominantly affect the C_m characteristics. One of the influential factors is revealed in the following section.

3.3 Relation to crater geometry

In this section, the influence of the formation of the crater on the impulse is investigated through crater analysis.

Past research reported that C_m has a single characteristic with ϕ_p variation in case of one given condition of the laser. However, effective fluence may be decreased during repetitive pulsed irradiation, which is caused by the formation and deepening of a crater. In order to calculate the effective fluence, ϕ_e, the crater shape generated by the repetitive laser pulse ablation was measured by a confocal laser microscope. The experimental conditions are shown in Table 3.3. For the purpose of comparison with the impulse result, the craters generated by a multiple of 25 pulses were measured. After removing obvious noise, the residual noise was removed from the data by low-pass filtering.

Figure 3.10 (a) shows a typical cross-section along the line from the center of symmetry at the entrance to the deepest point. D_c and h are defined as the crater diameter and crater depth, respectively. h_s is the slant height of the cone with the base of D_c and the height of h. The actual length of the cross-section, which has the same starting point and end point as h_s, is not a straight line and longer than that of h_s, as shown in Figure 3.10 (a). The maximum error is 8 %.

The effective crater surface area sharply changes with the deepening of the crater. At the beginning of repetitive irradiation, the ablator surface is flat. The area can be calculated as:

$$S_i = \pi\left(\frac{D_c}{2}\right)^2 \tag{3.6}$$

For repetitive irradiation, the shape of the crater can be assumed to be a circular cone, as shown in Figure 3.10 (b); thus the effective crater area for laser ablation corresponds to the lateral

area of the circular cone described by Eq. 3.8 below.

$$S_l = \frac{\pi D_c h_s}{2} = \frac{\pi D_c}{2}\sqrt{h^2 + \left(\frac{D_c}{2}\right)^2} \tag{3.7}$$

With the inclusion of the aspect ratio, $\alpha = h/D_c$, the effective fluence, ϕ_e can be calculated as:

$$\phi_e = \phi_p \frac{S_i}{S_l} = \phi_p \frac{\frac{D_c}{2}}{\sqrt{h^2 + \left(\frac{D_c}{2}\right)^2}} = \phi_p \frac{1}{\sqrt{4\alpha^2 + 1}} \tag{3.8}$$

Figure 3.11 shows ϕ_e decreasing with increasing E_t. Dotted curves exponentially fit to each experimental data. The black line shows typical threshold ablation fluence at 1.5 J/cm^2 [55]. ϕ_e decreases with repetitive irradiation (increasing E_t) and then becomes lower than the threshold fluence of ablation. This could be explained by the impulse with repetitive pulses becoming undetectable, because ϕ_e decreases to the ablation threshold. Figure 3.12 shows the relation of C_m and ϕ_e. In each ϕ_p condition, the ϕ_e is decreased with crater deepening caused by repeated ablation. In addition, the smallest C_m is obtained when ϕ_e decreases to around 2.0 J/cm^2. It is known that fluence has an ablation threshold. For an Al target ablated by a nanosecond pulsewidth laser, the ablation threshold is about 1.5 J/cm^2, similar to the results in our experiment. By using ϕ_e as a control parameter, the C_m complicated characteristics shown in Figure 3.9 exhibit a simple tendency, which increases rapidly to a peak and then gradually decreases with ϕ_e increment. This may indicate that all the parameters, except ϕ_e, accompanied by crater deepening, do not show outstanding effect on C_m. As a reference, C_m of a single pulse ablation of a planar surface under

vacuum by ablating an aluminum target with a Nd:YAG laser ,which has a wavelength of 1064 nm wavelength and a pulse width of 5 ns [31] is shown by gray colored plots in Figure 3.12. It should be noted that $\phi_e = \phi_p$ in the case of the reference because the ablator surface is flat. Maximum of C_m and C_m tendency, which quickly increases and then turn to decrease with increasing ϕ_p are consistent. However, the optimal fluence at which C_m becomes maximum in the reference (5.5 J/cm^2) is smaller than that of this research. While a burnt paper is used for determining *S*, the burnt area can be larger than the laser spot area caused by the low threshold of the burnt paper; thus, ϕ_p is estimated to smaller than that of this research.

Suzuki et al. [36] repetitively ablated POM against TEA CO_2 laser with a wavelength of 10.6 μm and a pulse-width (FWHM) of 140 ns, and reported that C_m increased to about 8% because of the pressure confinement with a sidewall in the presence of the crater. However, the enhancement of C_m is not observed in Figure 3.12. With the same ϕ_e, C_m of the first pulse (squared symbol) and that of the following pulses (circular symbol) are within a comparatively narrow range. If the enhancement C_m due to pressure confinement is outstanding, then C_m of the first pulse should be lower than that of the following pulses. Although, the cause is still unexpected, further investigation is beyond the scope of this study because the changing coincide with crater generation is not only due to the changing surface area and the pressure confinement with the side wall. Other factors such as oblique incidence, directionality of ablation impulse on the inner wall of the crater, and resolidification of melted Al ejected from the bottom region near the entrance of the crater, may all affect the impulse with repetitive irradiation.

Table 3.3 Experimental conditions for crater measurement.

Single-pulse fluence, ϕ_p [J/cm^2]	Total number of laser pulses, N_t
16	50, 100, 150
25	50, 75, 100, 150
29	50, 100, 150, 200
45	50, 100, 150
75	25, 50, 75

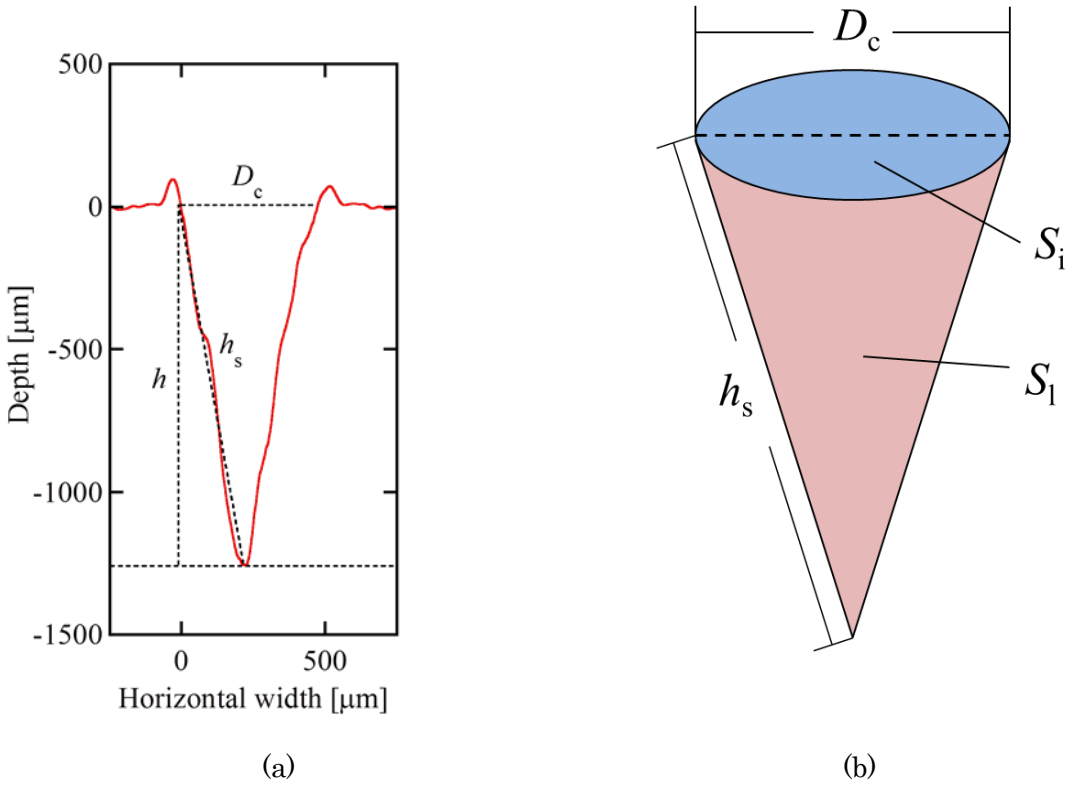

(a) (b)

Figure 3.10 (a) Example of a crater profile cross-section, N_t = 100, ϕ_p = 25 J/cm^2, (b) Schematic of a circular cone corresponding to the crater

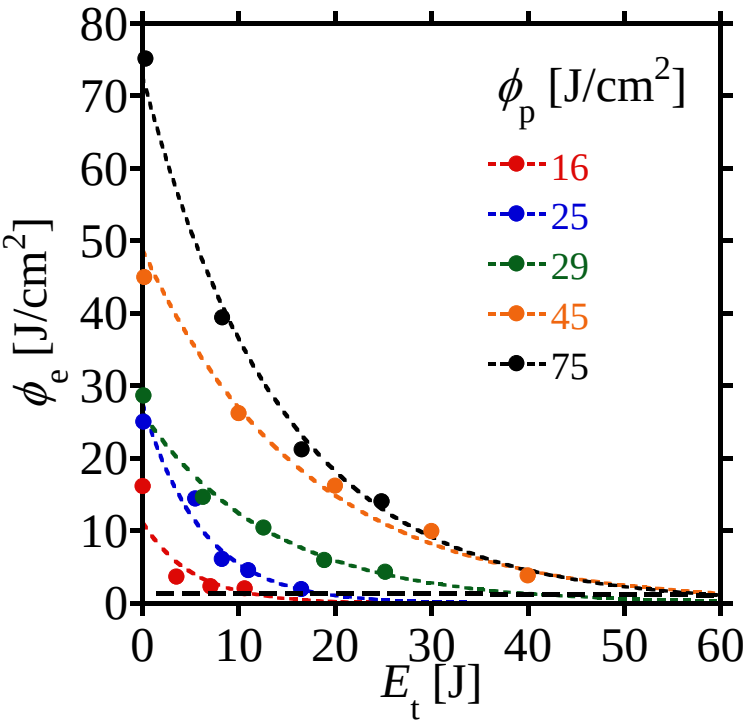

Figure 3.11 ϕ_e decrement with increasing E_t, Nd:YAG laser, λ = 1064 nm, τ = 7 ns, f < 0.1 Hz, laser spot area is 4.5×10^5 m^2, average in 4 runs in each condition.

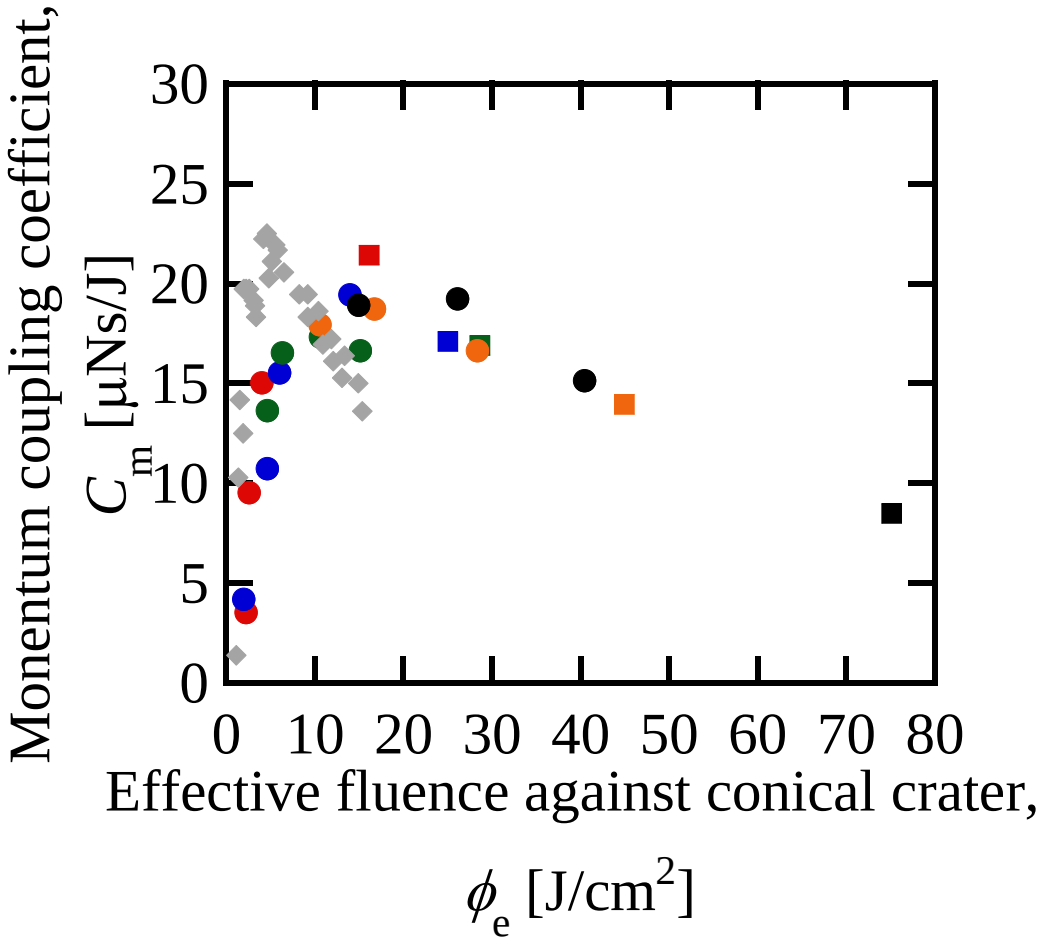

Figure 3.12 C_m dependence on ϕ_e, Nd:YAG laser; λ = 1064 nm; τ = 7 ns; f < 0.1 Hz; laser spot area = is 4.5×10^5 m^2; average of 4 runs in each condition; gray colored spots were obtained under vacuum by ablating an aluminum target with a single pulse of Nd:YAG laser, which has a 5 ns pulse width [31].

3.4 Conclusion

The impulse characteristics of an aluminum ablator against repetitive 1 μm wavelength, Nd:YLF laser pulses were investigated. ϕ_p significantly influenced the impulse in the range from 6 – 24 J/cm^2. I_m increased and reached saturation with increasing E_t. The saturation value of I_m increased with increasing ϕ_p. In applications such as microthruster technology or debris deorbiting, to keep the impulse large, it is necessary to move the laser-ablation spot to a fresh surface after appropriate laser pulses. This will prevent the generation of a deep crater that degrades C_m. The values of f and N_b did not lead to significant influence on I_m in the operation range examined. Not only C_m, but also $\bar{v}$ decreased with increasing N_t. The influence of an ablation-generated crater, which is deepened with repetitive pulsed irradiation of a 1064 nm wavelength Nd:YAG laser, on impulse was investigated. ϕ_e onto the crater inner wall was calculated by dividing ϕ_p by the increasing rate of the crater lateral area with repetitive irradiation, S_i/S_l. The relation of C_m and ϕ_e exhibits a simple variation as a function of ϕ_e, C_m sharply increases to a peak, and then gradually decreases as ϕ_e increases, eventually becoming undetectable because ϕ_e reaches the ablation threshold.

Chapter 4.
Impulse characteristics of polymers

The objective of this chapter is to clarify the impulse characteristics of polymers under a 1 μm high-repetition-rate solid-state laser. By fitting the experimentally measured impulse values to Phipps and Sinko's model in the vapor regime, the effective absorption coefficient during laser ablation will be evaluated.

First, the reference material for which the ablated area mainly depends only on the laser beam area is selected for measuring *S*. A previous paper [29] reported that C_m can be formulated as a function of $\phi_p \lambda \tau^{-1/2}$ where ϕ_p is a fluence, which is E_p divided by the laser irradiation spot area *S*. Using the same laser device, C_m depends only on ϕ_p. Thus, precise measurements of E_p and *S* are essential. In many previous studies, the actual ablated area on the material surface or burnt pattern on a sheet of thermosensitive paper was used to evaluate *S*. In this case, the ablated area by laser irradiation depends on the ablation threshold intensity of the material or thermosensitive paper. This becomes a technical problem when comparing the impulse characteristics among various materials. Therefore, it is necessary to evaluate *S* in a reasonable way.

Subsequently, using almost the same setup described in Chapter 3, the optical and impulse characteristics of polymers under the laser burst irradiation of Nd:YLF are investigated. The Phipps and Sinko model for a volume absorber in the vapor regime is used for evaluating the dominant parameter during laser ablation, which is accompanied by the absorption of the laser beam by a plasma. The dominant parameter for C_m will be cleared by fitting the theoretical equation to the experimental result.

4.1 Ablation spot area characteristics

Optically, the laser irradiation spot profile should be independent of ablation material and should depend only on the laser beam optics and irradiated energy. However, the laser beam profile on an ablation spot cannot be measured directly by a beam profiler because the focused beam intensity exceeds the damage threshold. Even by using a beam attenuator, in practice, the attenuation level is not uniquely adjusted among different laboratories; a large uncertainty in defining S and ϕ remains. The same problem arises when using thermosensitive paper. For this reason, in much of the laser ablation propulsion research, the laser ablation spot area, S, is defined as the area of a mark or crater, hereafter referred to as "crater," which is generated by laser ablation on the ablator itself. However, as will be presented later, the variation in laser ablation spot area strongly depends on the ablation material. It is necessary to develop a reasonable technique to quantify the laser spot area, which should generally be referred to and used.

Before investigating the impulse characteristics of polymers, we investigated the ablation spot area characteristics of various polymers. The objective of this spot area investigation was to choose a common reference material suitable for defining a laser spot area, thereby characterizing the laser ablation impulse characteristics of different materials with a common definition of laser spot area and fluence.

The first important aspect in practice is the dependence of the crater area on E_p. As the beam of the Nd:YLF laser used in this study is multimode of a nominal value of $M^2 = 1.5$, when at a small E_p level, the fluence in a peripheral part of the laser beam does not reach the ablation threshold; the crater area decreases. With increasing E_p, the portion where the local fluence exceeds the ablation threshold should increase, eventually becomes saturated to the whole beam cross-sectional area (Figure 4.1). In practice, as the fluence of the laser spot gradually decreases in such peripheral regions, it is not necessarily clear how to determine an effective ablation area.

What things become more complicated is that in some materials heat conduction around the laser spot significantly affects the crater formation, making a crater even larger than the laser spot itself. This issue should be carefully analyzed in the evaluation of the laser spot area.

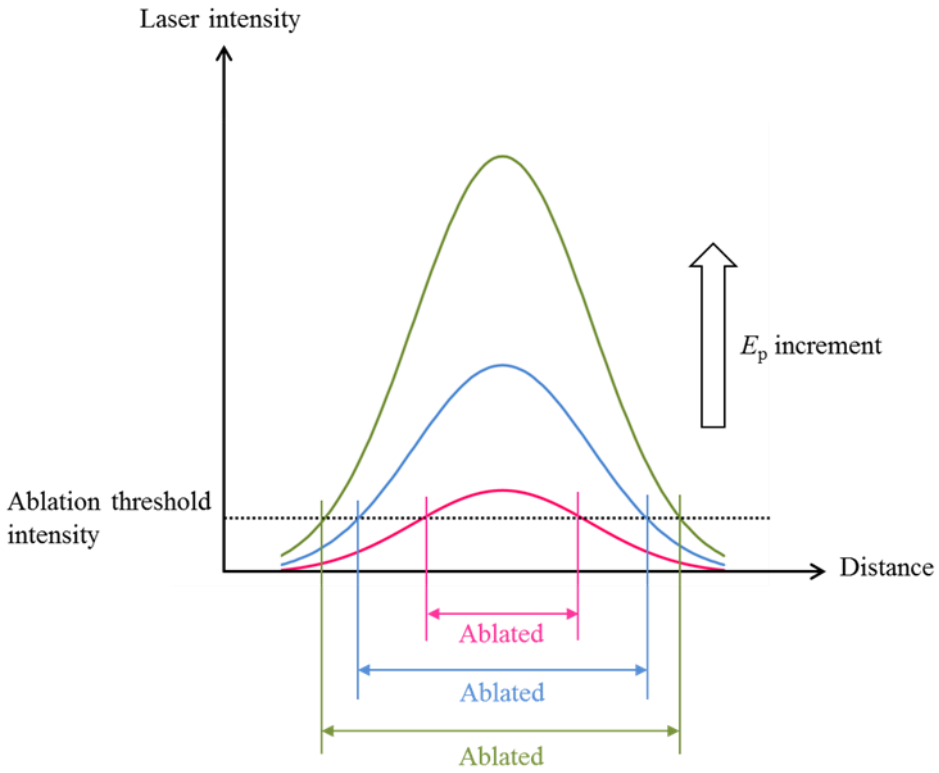

Figure 4.1 Schematic drawing of saturation of ablation diameter with increasing E_p, the energy distribution when focusing the Nd YLF laser used in this study is roughly arch shape that the peripheral decreases slowly.

The second point is the resolution of the crater area in the post-shot observation. If a fluence is moderate, the crater cannot be clearly observed with a small N_b. Once the crater becomes observable, the crater area somehow increases with increasing N_b, then saturates. The Nd:YLF laser has the special energy distribution in the shape of an arch that the peripheral decreases slowly. The center area of distribution is beyond the threshold intensity of ablation, while the peripheral is below the intensity. In the case of single pulse irradiation, only the center area is

ablated. Although the temperature increases by the absorption of the laser light, the peripheral area is not ablated. In the case of repetitive pulse irradiation, the peripheral area experiences intermittent rises in temperature and then melts. Therefore, the ablated area should saturate to the beam spot area. However, the actual ablated area becomes larger than the beam spot area caused by material properties such as the heat transfer coefficient and melting temperature. The degree of area expansion depends on the material. Therefore, it should be carefully determined if the crater area has a saturated value, which is obtained with a sufficient number of laser pulses.

From the above-mentioned aspects, we surveyed the characteristics of laser ablation crater formation with various polymers and aluminum to find an appropriate reference material to define *S*. The criteria for the reference material are as follows:

1. With increasing E_p, *S* should be saturated.
2. The crater should be observed even at small E_p.
3. A thermally affected area around the laser beam, in which the material is melted by thermal conduction or the ejected material from the crater is piled up, should be sufficiently small. *S* should be saturated with increasing N_b.
4. The crater should not be accompanied by cracks.
5. The material characteristics can be reproduced anywhere, and do not depend on production processes.

In order to select a reference material satisfying these criteria using a Nd:YLF laser (λ: 1047 nm, τ: 5 – 15 ns (FWHM)), the following materials were examined: polycarbonate (PC), polyethylene terephthalate (PET), polyvinyl chloride (PVC), aluminum (A1050), Carbon Fiber Reinforced Plastic (CFRP), polytetrafluoroethylene (PTFE or TEFLON®), polyimide (PI or KAPTON®), polypropylene (PP), polyoxymethylene (POM), polyamide (PA), and polymethyl

methacrylate (PMMA). The same experimental setup as shown in Figure 2.1 was used while the test material was mounted on one end of the impulse pendulum arm in the vacuum chamber, as was performed in the impulse measurement. The distance from the achromatic lens with a focal length of 150 mm to the material surface was set to 138 mm. S was measured using a confocal laser scanning microscope (horizontal resolution: 0.01 μm, height resolution: 0.01μm, VK-9500, KEYENCE Company). The edge of the region that is darker than the original surface is traced manually. S is defined as the area bounded by a trace line.

With respect to the criteria 1 and 2, the dependence of S on E_p was measured after $N_b = 1000$ pulses, each with E_p varying from 0.72 – 8.06 mJ. Photographs of the craters for two or three E_p values are shown in Figure 4.2 and Figure 4.3. The tested materials are divided into two groups.

For the materials displayed in Figure 4.2, S somehow becomes saturated with increasing E_p. The burnt surface of aluminum and CFRP is elliptical; it better reproduces the actual laser beam shape, which has an ellipticity of 0.7. In the case of $E_p = 5.03$ mJ for CFRP, both the resin and fiber are evaporated in the central black region. In the peripheral, only the surface resin is evaporated while the fibers remain because of their higher boiling point. With a further increment of E_p to 7.48 mJ, the fiber-exposed peripheral is extended only in the fiber alignment direction. This indicates that the heat conductivity in the fiber alignment direction is higher than that in the transverse direction.

The materials in Figure 4.3 have unsaturation tendencies. The shape of the burnt surface of PC, PET, and PVC approximately resembles a circle. This is because the peripheral of the ablated region is melted or evaporated because of the heat conduction from the ablation region and/or radiation from the ablation plume. In the present experiments, these polymers had machining patterns with an interval of 10 – 100 μm on its surface. Yet, with burst mode irradiation in this study, the machining pattern in the laser spot was removed with just a few pulses; the profile of the irradiated surface continued changing during the burst. Therefore, the effect of the machining

pattern on S and the impulse was negligible. In Figure 4.3(d), the melted PI remains around the central evaporated part. The thickness of the melted peripheral part increases with E_p. In Figure 4.3(e)-(g), the burnt pattern is not observed when E_p < 3 mJ, indicating that laser fluence is insufficient for ablating these polymers. The boundary of the ablated area of PP is unclear. With PMMA in Figure 4.3(h), the crater is accompanied by the formation of cracks in random patterns. As it is difficult to determine a boundary clearly, there is some ambiguity when measuring S.

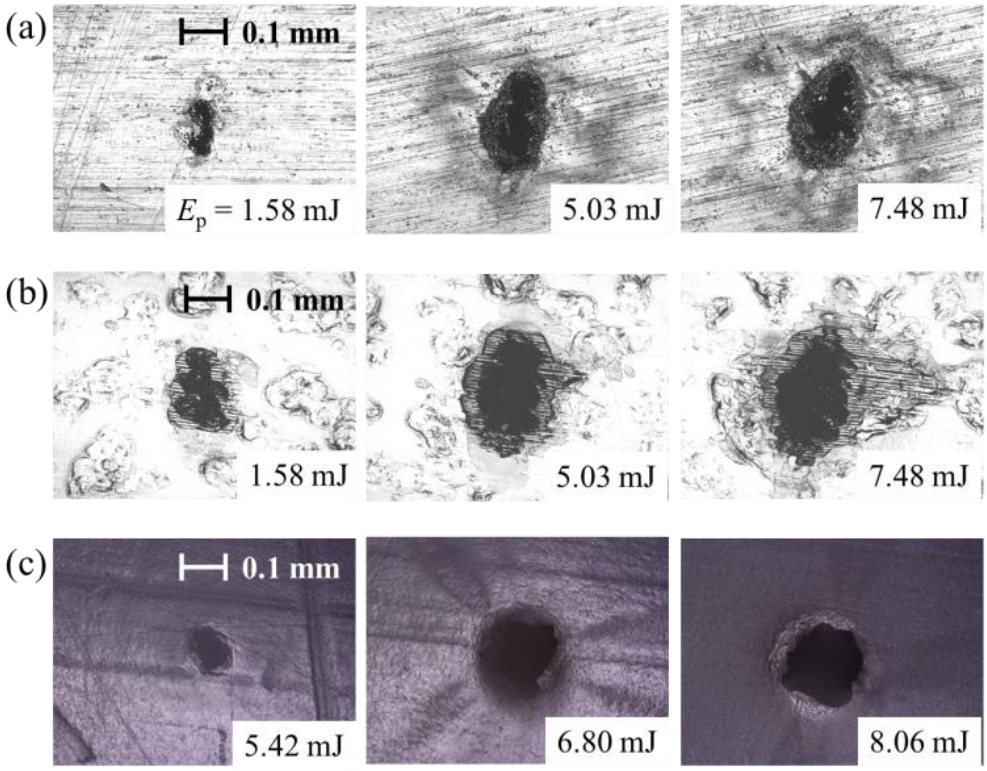

Figure 4.2 Microscope photographs of ablated area with different E_p, with S saturating with increasing E_p, (a) aluminum, (b) CFRP, and (c) PTFE.

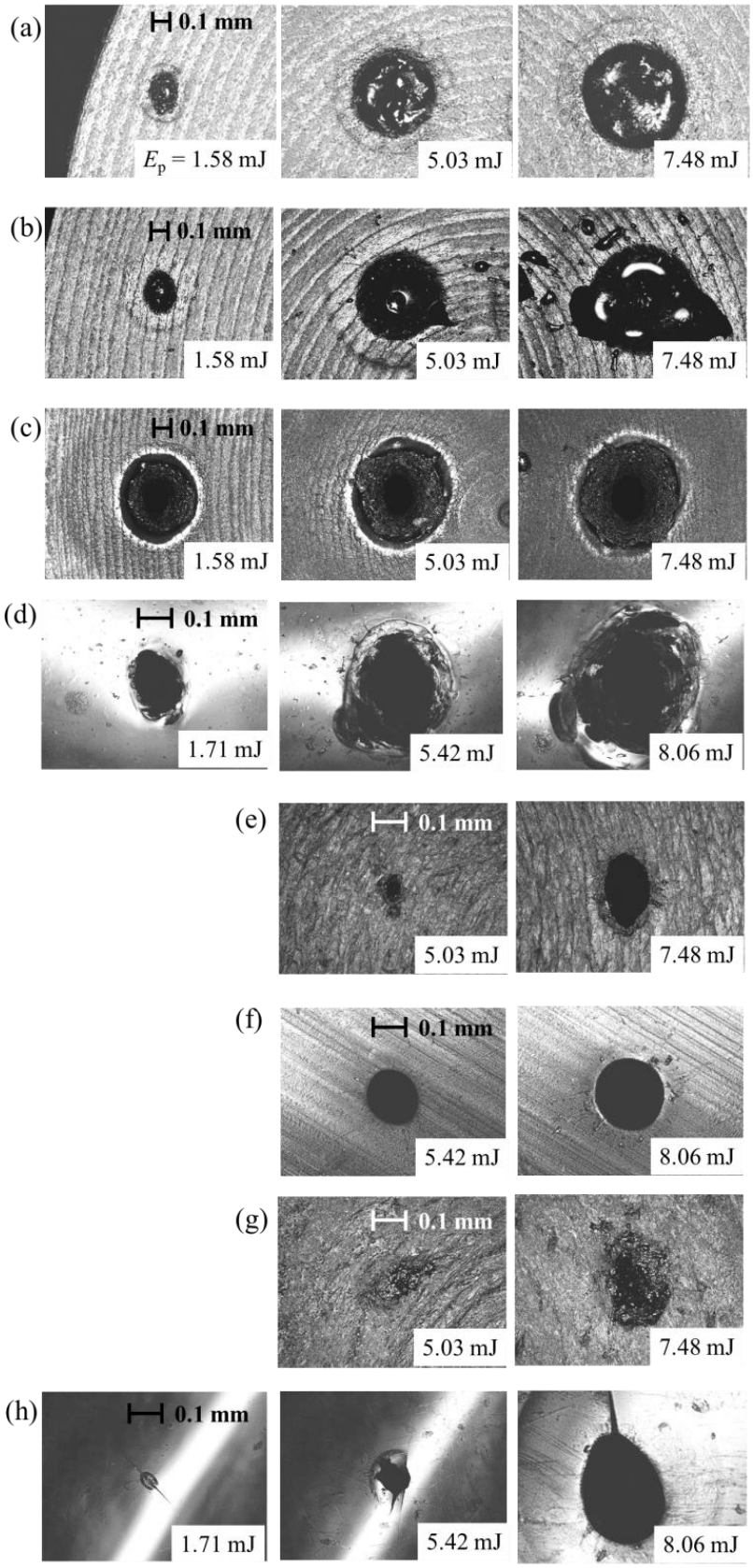

Figure 4.3 Microscope photographs of ablated area with different E_p, with S not saturating with increasing E_p, (a) PC, (b) PET, (c) PVC, (d) PI, (e) PA, (f) POM, (g) PP, and (h) PMMA.

Figure 4.4 displays the dependence of S on E_p. Figure 4.4(a) shows the variations in the small S materials with S smaller than 1×10^5 μm^2. S for Aluminum, CFRP, and PTFE become saturated, satisfying the criterion 1. With aluminum, CERP, PC, PET, PVC, PI, and PMMA, ablation occurs even when E_p is smaller than 2 mJ, thereby the criterion 2 is satisfied. Figure 4.4(b) shows the variations in the large S materials; in all the materials S increases with E_p in this range. With all the polymers in this group ablation occurs even with E_p is smaller than 1 mJ, satisfying the criterion 2.

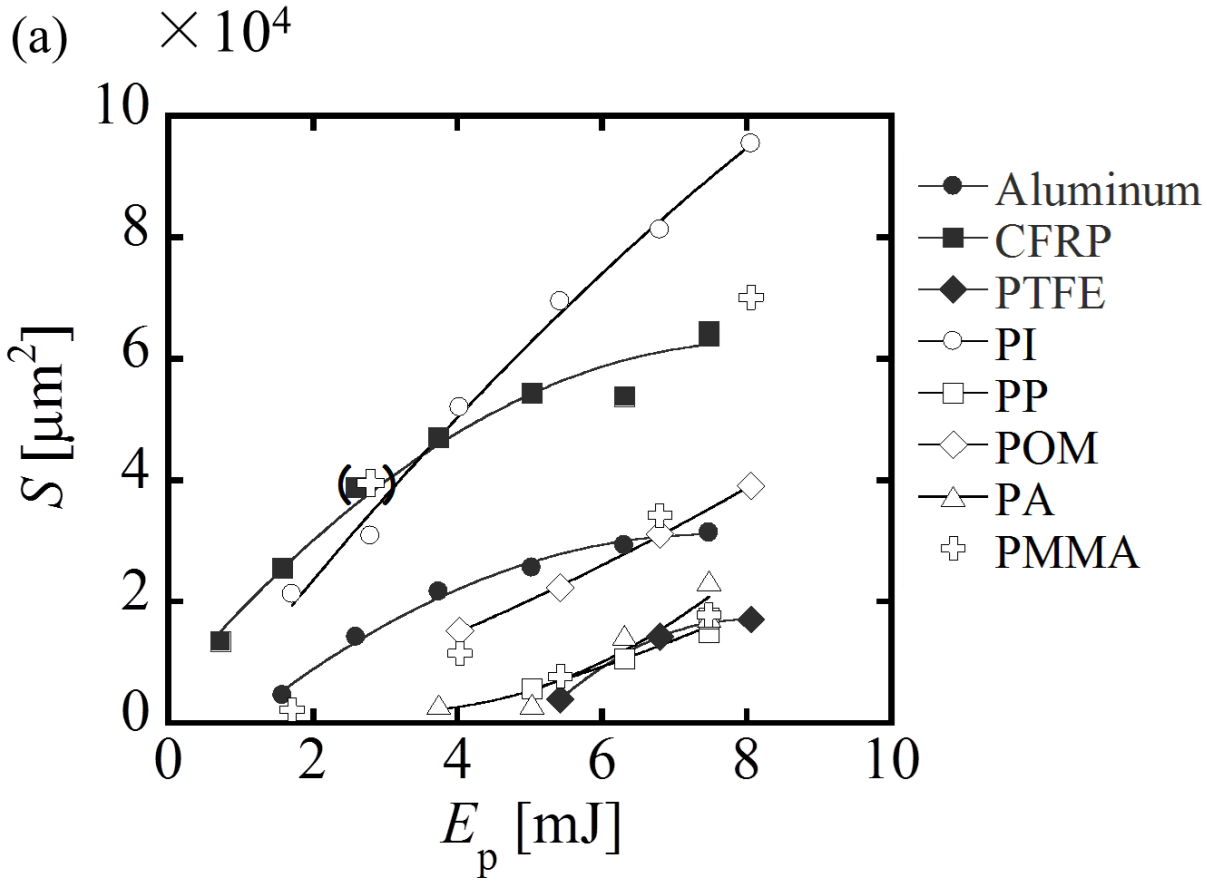

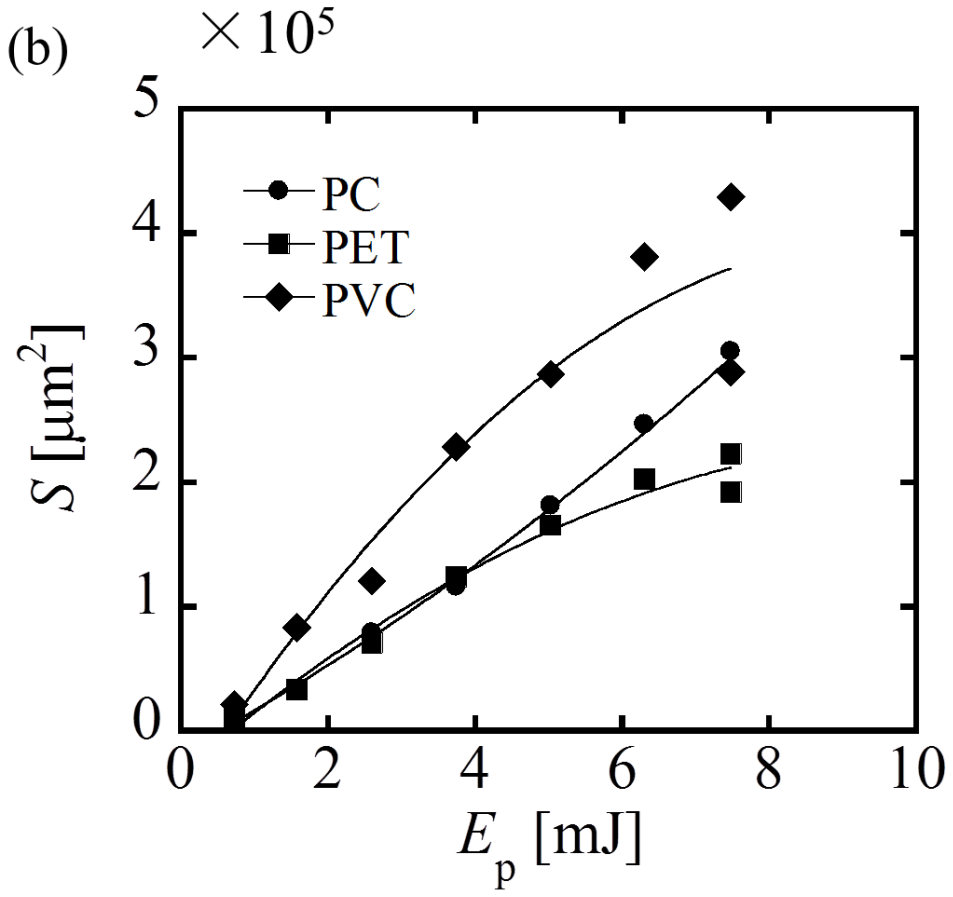

Figure 4.4 The dependence of S on E_p with N_b = 1000 pulses and f = 1 kHz for (a) small S materials and (b) large S materials.

In order to examine the criterion 3, the dependence of the ablated area on N_b was measured. N_b was varied, with values of 10, 50, 100, 200, 500, and 1000 while E_p was set to a constant 7.48 mJ. The tested materials were categorized into two groups.

In the saturated group of Figure 4.5, S with N_b = 1000 ranges from $1.5 \times 10^4 - 6.5 \times 10^4$ μm^2. In N_b = 10 of Figure 4.5(a), the color of the ablated area is white, which is because the crater depth is shallow. With increasing N_b, the color becomes darker because of crater deepening. The ablated area does not increase during the deepening. In the not saturated group of Figure 4.6, S with N_b = 1000 ranges $1.9 \times 10^5 - 4.2 \times 10^5$ μm^2. The ablated area at N_b = 10 is small and elliptical. With increasing N_b, the ablated area increases and becomes almost circular.

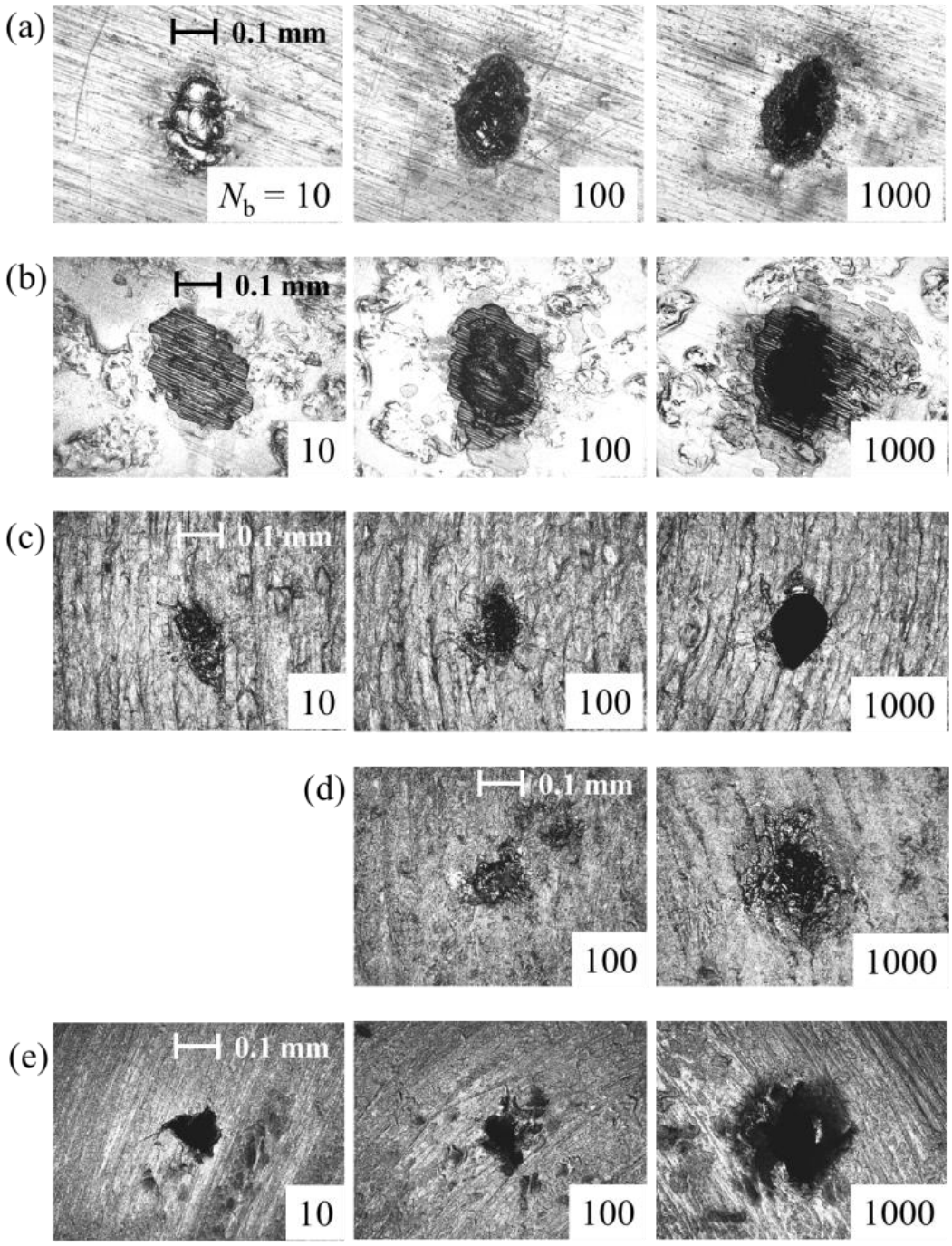

Figure 4.5 Microscope photographs of ablated area with different N_b, with S saturating with increasing N_b, (a) aluminum, (b) CFRP, (c) PA, (d) PP, and (e) PMMA.

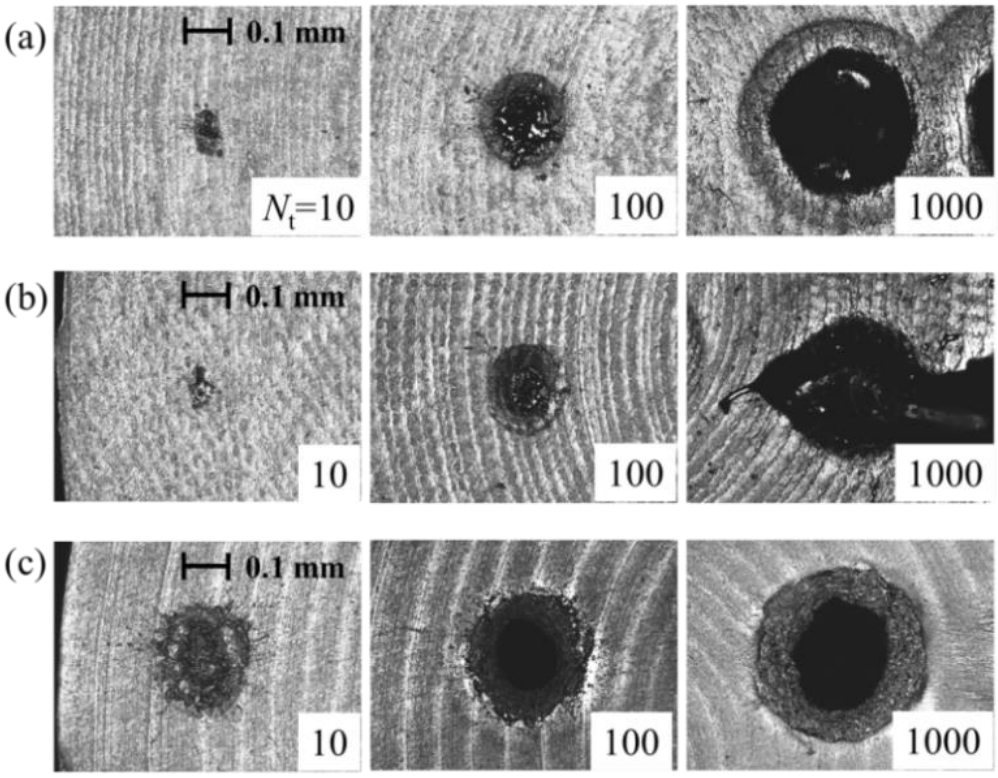

Figure 4.6 Microscope photographs of ablated area with different N_b, with S not saturating with increasing N_b, (a) PC, (b) PET, and (c) PVC

Figure 4.7(a) and (b) display the dependence of S on N_b in the respective groups. The materials with small S of Figure 4.7(a), S of aluminum and CFRP is saturated even when $N_b < 100$, and is kept almost constant with further increments of N_b. Although S of PA and PP slightly increases with N_b, the increment is smaller than 1×10^4 μm^2. Therefore, aluminum, CFTP, PA, and PP satisfy the criterion 3; S becomes almost constant with a sufficient number of pulses for $100 < N_b < 1000$. S of Figure 4.7(b) do not saturate within this N_b range.

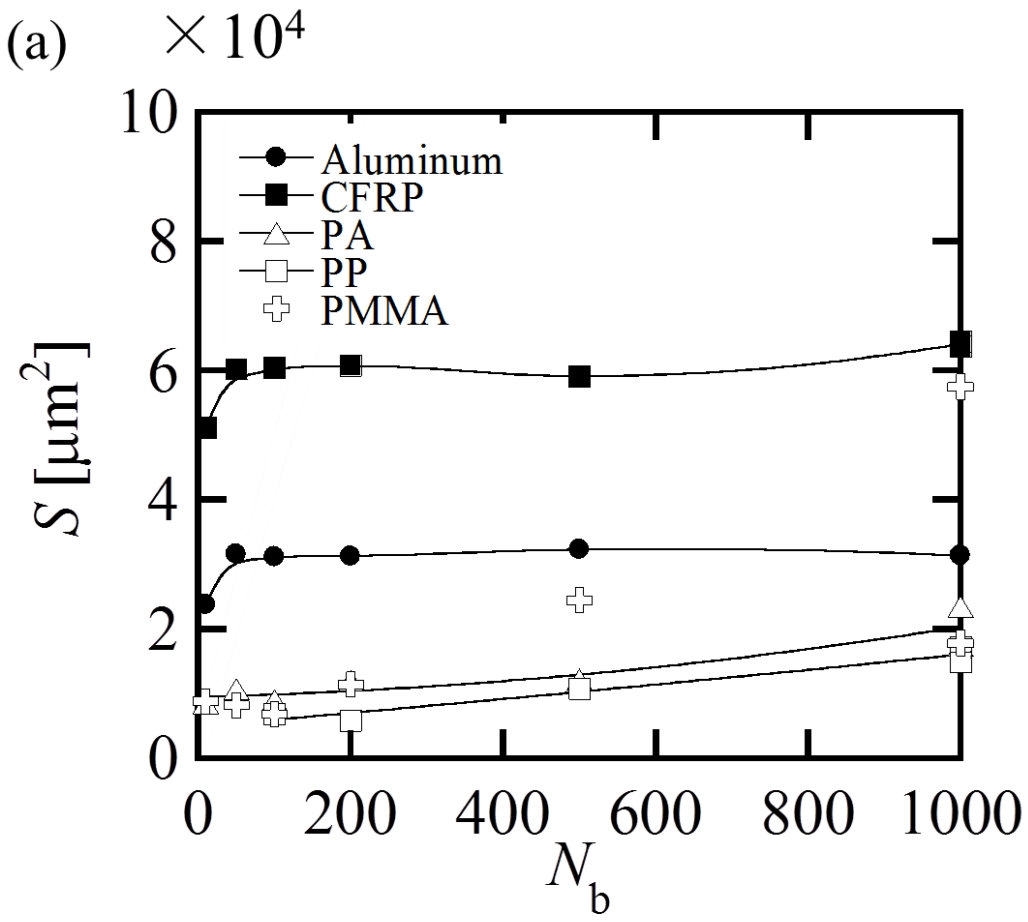
(a)
×10^4
10
8
6
4
2
0
S [μm^2]
Aluminum
CFRP
PA
PP
PMMA
0
200
400
600
800
1000
N_b

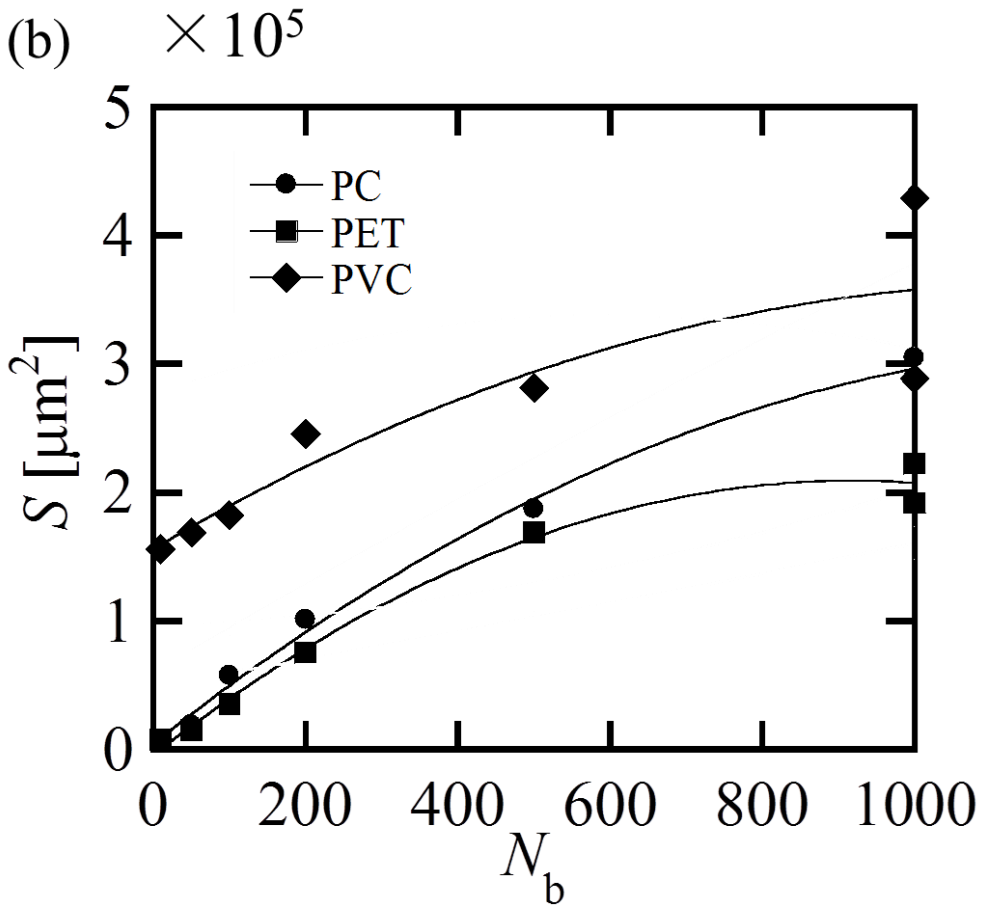

Figure 4.7 Dependence of S on N_b with E_p = 7.48 mJ and f = 1 kHz for (a) small S materials and (b) large S materials.

The summary of the material survey is presented in Table 4.1. In the table, "Y," blank, and "N/A" indicate that the criterion is satisfied, not satisfied, and data note available, respectively. Although CFRP satisfies the criteria 1 to 4, its mechanical property depends on the matrix structure, type of carbon fiber and resin, and even production processes; therefore, the criterion 5 is not satisfied and not suitable as the standard material. All the polymers except PMMA satisfy the criteria 4 and 5. However, the polymers are not suitable as the standard material because none

of them satisfy all of the criteria from 1 to 3. Most of the polymers do not satisfy the criterion 1 because their boiling point is not sufficiently high, and the peripheral of the laser irradiation area is melted or evaporated. Aluminum, however, is the only material satisfying all the criteria. Therefore, in this study, aluminum was selected as the reference material to evaluate *S*. In the following experiments with burst irradiation, single pulse fluence, ϕ_p is uniquely defined for all materials as the ratio of E_p to *S* that is obtained with aluminum as the saturated value for increasing N_b.

Table 4.1 Summary of the standard material selection.

Criteria	Al	CFRP	PTFE	PC	PET	PVC	PI	PA	PP	PMMA	POM
1	Y	Y	Y								
2	Y	Y		Y	Y	Y	Y			Y	
3	Y	Y	N/A				N/A	Y	Y		N/A
4	Y	Y	Y	Y	Y	Y	Y	Y	Y		Y
5	Y		Y	Y	Y	Y	Y	Y	Y	Y	Y

4.2 Impulse characteristics and effective optical properties

4.2.1 Optical property of polymers without ablation

Here, five polymers and aluminum (1050A) were selected to evaluate impulse characteristics. POM and PTFE are milky-white crystalline polymers, while PMMA, PC, and PET are transparent amorphous polymers. Prior to measuring an impulse, the optical property of these polymers without ablation at λ = 1047 nm was experimentally tested at the atmospheric pressure and room

temperature. The Nd:YLF laser beam of E_p = 6.80 mJ and f = 1 kHz was sent through the polymer test plate without being focused by a condensing lens and then irradiated onto the power meter (F150A-SH-V1, OPHIR). Five plate thicknesses (1, 3, 5, 8, and 10 mm) were examined to each material. Because the power meter takes a few seconds to rise, the time duration of a single burst was set to 10 s and the value after 5 s was recorded. Virgin surfaces that were commercially delivered were used without any special treatment such as polishing. Because the incident laser beam was unfocused with a diameter of 4 mm, ϕ_p on the material surface was 4.6×10^{-5} J/cm^2, roughly five orders of magnitude smaller than a typical ablation threshold. After this measurement, any damage was not visibly found on the test material surface.

The experimentally acquired optical properties are shown in Figure 4.8. The transmittance without ablation at a material thickness of x mm, $T_i(x)$ is the ratio of power pass through the plate to power of without plate. For estimating the absorption coefficient without ablation, α_i, the curves are fit to the Beer's law equation as

$$T_i(x) = T_i(0)exp(-\alpha_i x) \tag{4.1}$$

where $T_i(0)$ is the transmittance on the surface, and is equal to 1-R (R: reflectance). With the transparent polymers, $T_i(0)$ ranges from 0.91 to 0.93, α_i is as small as 2 to 4 m^{-1}. Conversely, $T_i(0)$ of the white polymers ranges from 0.21 to 0.24, with α_i larger by a factor of 40. The values of $T_i(0)$ and α_i of each material are summarized in Table 4.2.

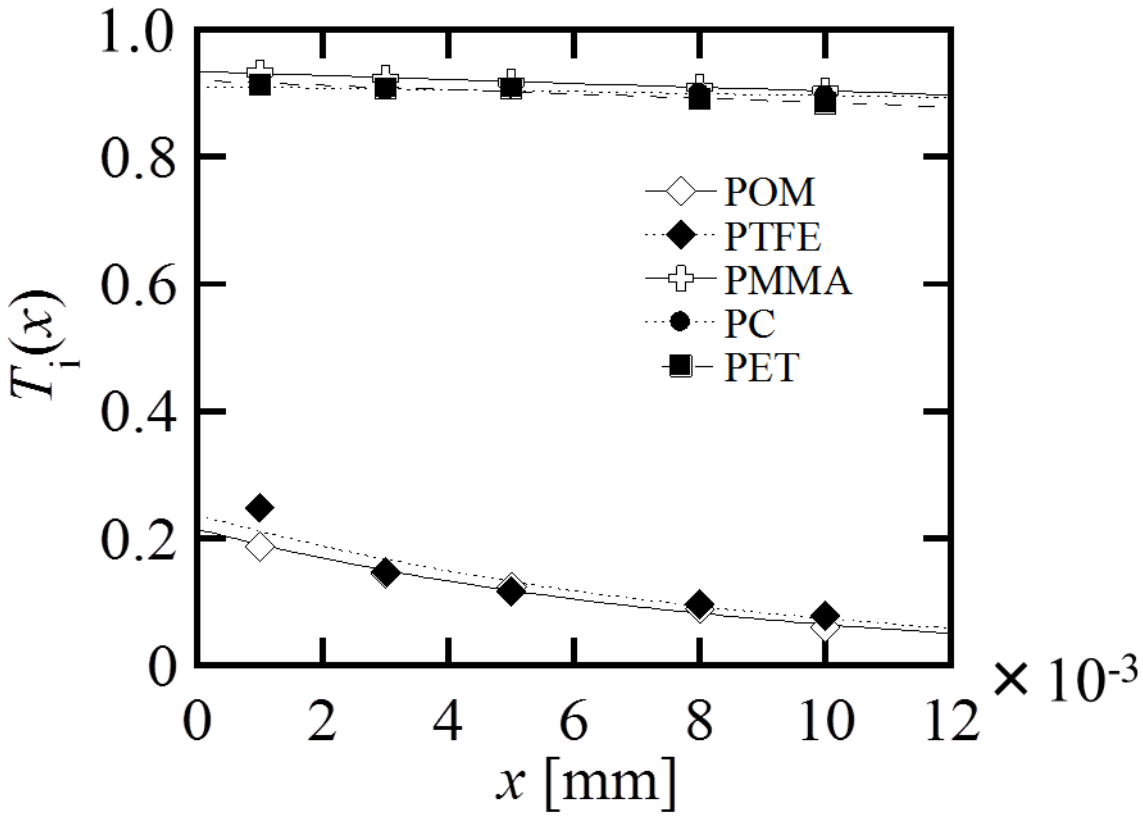

Figure 4.8 Optical property of polymers without ablation.

Table 4.2 Coefficients included in Eqs. 4.1, and 4.5.

		without ablation		with ablation	
	ρ	$T_i(0)$	α_i	ϕ_t	α_a
	kg/m^3	-	1/m	J/m^2	1/m
POM	1410	0.21	119	1.0×10^5	9.6×10^5
PTFE	2200	0.24	116	1.1×10^5	1.5×10^5
PMMA	1190	0.93	3	8.0×10^4	1.1×10^7
PC	1200	0.91	2	6.5×10^4	3.4×10^6
PET	1270	0.92	4	6.0×10^4	2.7×10^6

4.2.2 Ablation impulse characteristics

An elementary process of laser-material interaction is the excitation of electrons by electromagnetic waves of a laser beam. Electrons to be excited are either bounded by molecular or lattice energy or free from such bond energies. Yet, such free electrons can better absorb laser energy when their oscillation starts to resonate with an exciting electromagnetic field. "Seed" free electrons can be generated either from a statistical energy distribution or a contaminant with a low electron affinity, or other causes. Whatever their origins are, once such electrons are generated, they efficiently absorb the proceeding laser power to induce additional ionization. This phenomenon is known as "electron avalanche." Once it happens, the optical properties of the matter over the surface greatly change because of plasma formation[58]. The resulting interactions between the ablator and laser beam are complicated depending on the various conditions including material, surface condition, temperature, laser energy, wave length, beam profile, and temporal intensity variation. In applications for laser ablation propulsion, Sinko and Phipps[40] categorized the operation regime into "vapor" and "plasma" regimes. In the vapor regime, an ablator surface is heated by laser power so that the material in the laser spot is melted and evaporated under supercritical pressure, thereby yielding a large impulse. In this regime, C_m becomes an increasing function of fluence. Yet, at a critical value of fluence, which depends on the material and laser conditions, C_m becomes saturated and begins to decrease, the condition of which corresponds to the plasma regime. In this regime, part of the laser beam power is not transmitted to the ablator because of the shielding by plasma generated above the ablator surface[46]. The greater the laser power, the stronger the plasma shielding effect, and the smaller the C_m. The quantitative characteristics of those impulse behaviors strongly depend on the material and laser conditions. With polymer materials, in spite of its importance little has been known about such impulse characteristics.

The impulse measurements were conducted using the setup illustrated in Figure 2.1. The

torsion-type impulse pendulum was placed in a vacuum chamber, 0.7 m in diameter and 2.2 m in length. The vacuum chamber was evacuated to an ambient pressure of 2×10^{-2} Pa by a turbo molecular pump (2000 L/s, TMP-2003LM, Shimadzu co.) backed by a rotary pump (533 L/s, T2033SD, Alcatel). The output pulse from a Nd:YLF laser with a λ of 1047 nm and a τ of 5 – 15 ns was initially sent into the vacuum chamber through a BK7 window and then focused by a 150 mm focal length achromatic lens onto the ablator. The 18-μm-thick cellophane film was placed just behind the beam condensing lens with an oblique angle of incidence of 30° to avoid contaminating the lens against the exhaust ablation plume. The T_i of the film corresponding to the 1047 nm pulse was measured to be almost 99 %. The beam angle of incidence was 90° with an error less than 5°. With laser pulse irradiations, the laser-ablated plume was ejected normal to the ablator surface, which induced the torsion pendulum arm to oscillate. The temporal deflection of the arm tip was measured using a linear variable differential transformer (resolution: 0.29 V/mm, Model 1591ST, Shinko Electric co.) and recorded by a digital oscilloscope. The calibration of the torsion impulse stand and data analysis process are described in a previous paper [50]. The E_p used in the experiment was in the $1.56 \leqq E_p \leqq 9.45$ mJ range. The distance between the lens and the ablator surface was set to 136, 138, and 140 mm to vary S values. The range of ϕ_p was $6.5 \leqq \phi_p \leqq 16.7$ J/cm^2. f was set to a constant of 1 kHz.

Figure 4.9 displays the dependence of C_m on ϕ_p up to 17.5 J/cm^2. Each point refers to an average of three to five burst shots. Although not shown in the figure, the typical standard deviation is smaller than 1 μNs/J except for PMMA. However, in the case of PMMA, cracks were formed randomly; the standard deviation was quite large, ranging even to 12 μNs/J. The C_m of all the polymers increase with ϕ, corresponding to the vapor regime. Yet, the C_m of aluminum has a maximum of 16.1 μNs/J at ϕ = 9.6 J/cm^2 and then decreases in the plasma regime because of plasma shielding. The threshold fluence for ablation, ϕ_t, and the increasing rate of C_m depends strongly on the material. The values of ϕ_t for the “transparent” polymers (PMMA, PC, and PET)

have ϕ_t close to that of aluminum, around 7 J/cm^2. Even for ϕ_p increasing past the critical value for aluminum, C_m of those polymers continue to increase in the vapor regime. With the "white" polymers (POM and PTFE), ϕ_t are higher than those of the transparent polymers, around 10 J/cm^2. The rate of increase of C_m with respect to ϕ_p is highest with PTFE, with C_m having a maximum of about 60 μNs/J in this range. With PMMA, however, the rate of increase of C_m remained lowest among the polymers examined here. Nevertheless, for ϕ_p >13 J/cm^2, C_m with all the polymers were higher than that of aluminum. The presented impulse characteristics should be closely related to the effective optical properties with laser ablation, the details of which will be analyzed in the next section.

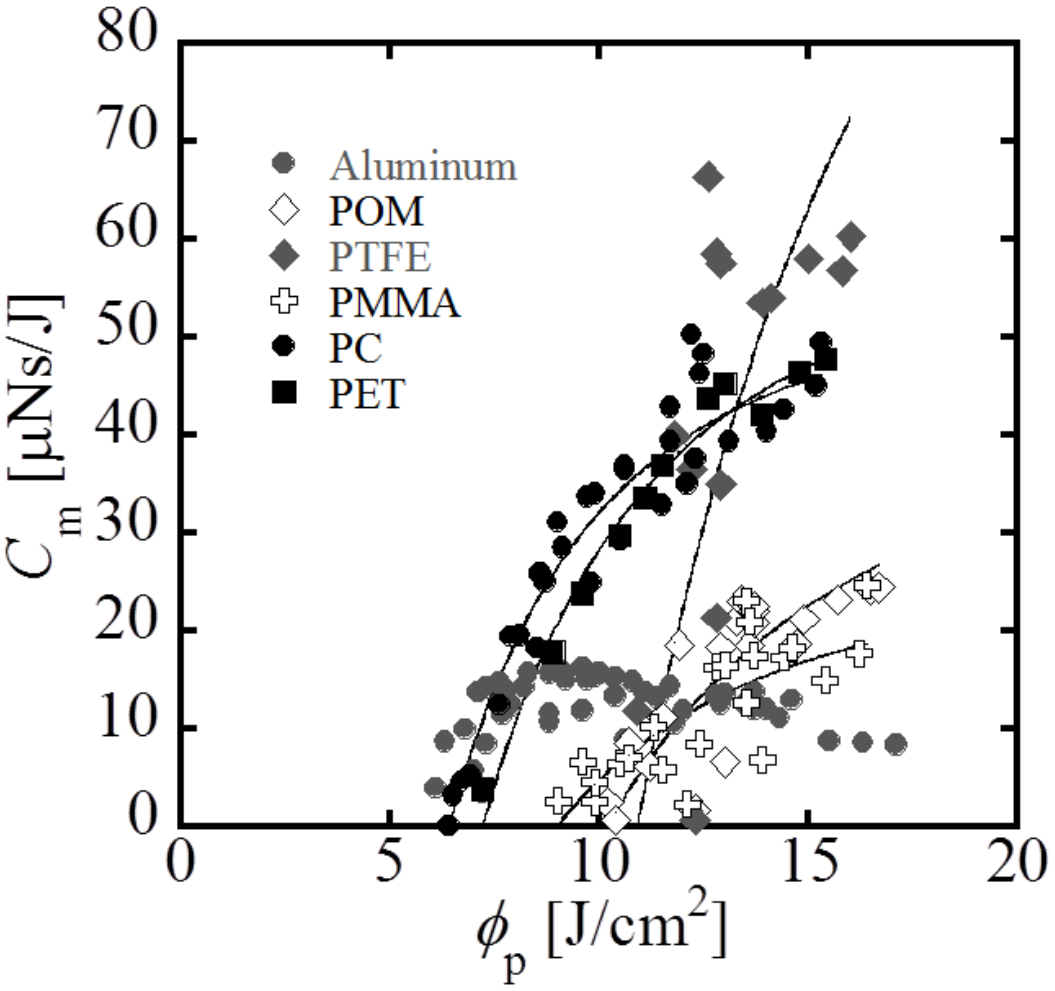

Figure 4.9 Dependence of C_m on ϕ_p with f = 1 kHz and N_b = 200 pulses. Solid lines fit to Equation 4.5 by the method of least squares.

4.2.3 Effective optical properties for impulse generation

Even in the vapor regime, the processes of laser power absorption are quite different from those without ablation because the role of free electrons is dominates. As a result, the effective absorption coefficients during laser ablation, α_a, are quite different from those without ablation, α_i. A part of the deposited laser energy is consumed for the latent heats of the ablator, yet a much larger amount of energy is converted to kinetic energy of the ablated mass, thereby affecting to an impulse. Sinko and Phipps [46] proposed a model equation for C_m to evaluate α_a based on Beer's law for a volume absorber in the vapor regime. $T_a(0)$ ϕ_p of energy penetrates into a material. The

energy decreases by depth according to Beer's law and then reaches $T_a(0)\ \phi_t$ at d_a (Figure 4.10). It should be noted that both ϕ_p and ϕ_t are defined at the ablator surface before reduction by reflection. The relational expression as

$$\phi_t = \phi_p 10^{-\alpha x_a} \tag{4.2}$$

$T_a(0)$ is not shown because this coefficient exists in the both sides. The exhaust mass areal density by laser ablation as

$$\mu = x_a\ \rho = \frac{\rho}{\alpha_a} ln \frac{\phi_p}{\phi_t} \tag{4.3}$$

Energy conservation per unit area as

$$\frac{\sigma^2}{2\mu} = T_a(0)\left(\phi_p - \phi_t\right) \tag{4.4}$$

where σ is momentum per unit area. From Equation 4.3 and 4.4,

$$C_m = \frac{\sigma}{\phi_p} = \sqrt{\frac{2\rho T_a(0)}{\alpha_a \phi_t} \times \frac{\xi - 1}{\xi^2} \times ln\,\xi} \tag{4.5}$$

$$\xi = \frac{\phi_p}{\phi_t} \tag{4.6}$$

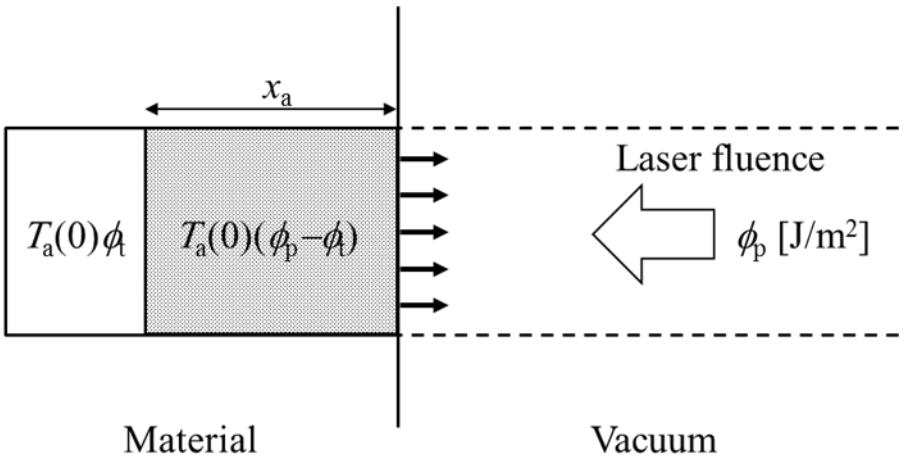

Figure 4.10 Absorption of the laser fluence to the volume absorber.

Equation 4.5 should be fit to an experimentally-measured C_m-ϕ_p relation where $T_a(0)/\alpha_a$ and ϕ_t are fitting parameters. ϕ_t is determined as the intercept on the ϕ_p coordinate in Figure 4.9. However, from the experimental relation, $T_a(0)$ and α_a cannot be determined independently; only their ratio becomes an independent fitting parameter. Here, we assume that $T(0)$ remains constant even with ablation ($T_a(0) = T_i(0)$) because its order of magnitude does not change even with ablation[59,60]. Only the value of α_a was determined from the least squares method. The fitting result for each material is indicated by a solid curve in Figure 4.9. As observed in Table 4.2, α_a becomes three to six orders of magnitude larger than α_i. The range from the ablation threshold to the optimal fluence is in the vapor regime[46]. Even within this range, free electrons essentially play an important role in the laser power absorption processes[61]. The plasma density gradually increases with fluence. This extremely high value of α_a should be achieved by the absorption of the incident laser power by the plasma. Makropoulou et al. [59] measured the etch rate of ablation

induced by a Q-switched Nd:YAG laser (λ : 1.064 μm, τ : 25 ns, f < 1 Hz) and estimated α_a from fitting to experimentally obtain the etch rate to the relational expression from Beer's law, thereby obtaining $\alpha_a = 3.1\times10^4$ m^{-1} for PTFE, the order of magnitude of which agrees with the present experiment. The difference by a factor of five should be due to the different experimental conditions such as ambient pressure, pulse number, and laser spot size. PTFE achieved the highest C_m of 66 μNs/J. α_a of PTFE is more than six times smaller than that of the other polymers, while the differences in other parameters, ρ, $T_i(0)$, and ϕ_t, are within a factor of four. Therefore, PTFE exhibited the best performance as a volume ablator in which a large amount of mass is ablated because of a relatively small value of α_a, which corresponds to a large absorption depth, $1/\alpha_a$, thereby yielding the highest C_m.

4.3 Conclusion

In this study, the ablation spot area and impulse characteristics of polymers were investigated against a Nd:YLF laser burst with a pulse repetition rate of 1 kHz, wavelength of 1047 nm, and a pulse width of 5 –15 ns. Aluminum (1050A) was employed as the reference material to evaluate the crater area and fluence because its crater area variation indicated reasonable dependences on the number of laser pulse irradiations and laser pulse energy. POM and PTFE as milky-white crystalline polymers and PMMA, PC, and PET as transparent amorphous polymers were used in measuring an impulse. The range of ablation thresholds of transparent polymers was 6 J/cm^2 to 8 J/cm^2, which is lower than that of the milky-white polymers (10 J/cm^2 to 11 J/cm^2). The operation was in the vapor regime in which C_m continued to increase with fluence, thereby attaining a maximum C_m of 17.5 J/cm^2. The C_m of all the polymers examined here exceeded the maximum value obtained with aluminum, 18 μNs/J. This results suggest promising applications of laser

ablation to space propulsion including deorbiting and de-tumbling space debris using polymers and 1 μm laser pulses, which is obtained by diode and fiber lasers. By fitting the C_m equation to the experimental result, the effective absorption coefficient during laser ablation was estimated to be three to six orders of magnitude larger than that without ablation. The maximum C_m, 66 μNs/J, was obtained by PTFE with an effective absorption coefficient more than six times smaller than that of the other polymers. This result indicates that α_a is the dominant parameter for C_m. A smaller α_a is equivalent to a deeper absorption depth, $1/\alpha_a$, thus indicating a larger ablation volume. A larger ablation volume contributes to the enhancement of C_m.

Chapter 5.
Conclusions

From the investigation of impulse characteristics induced by repetitive laser pulse irradiations depending on laser operation and material conditions, the following conclusions are obtained.

The impulse characteristics of an aluminum ablator against repetitive Nd:YLF laser pulses with a 1047 nm wavelength and 5 – 15 ns pulsewidth were investigated. The integrated impulse increased, and then it gradually reached saturation as the total laser energy increased. In the operation range examined, the saturation value of the impulse increased with increasing single-pulse fluence. The relationship between impulse and crater formation on an aluminum ablator with repetitive irradiation of Nd:YAG laser pulses (wavelength of 1064 nm, pulse duration of 7 ns) is investigated. Surface area changes caused by crater deepening are measured with a laser microscope, then used for calculating the effective fluence. The fluence is compared to a corresponding variation in the momentum-coupling coefficient with repetitive pulses. The relation of momentum-coupling coefficient and effective fluence fits to a simple variation; that is, it sharply increases to a peak value as the effective fluence increases, then gradually decreases. This is strong evidence that the effective fluence is one of the main parameters for deciding the momentum-coupling coefficient.

The ablation spot area and impulse characteristics of polymers were investigated against a Nd:YLF laser burst with a pulse repetition rate of 1 kHz. Aluminum (1050A) was employed as the reference material to evaluate the crater area and fluence because its crater area variation indicated

reasonable dependences on the number of laser pulse irradiations and laser pulse energy. POM and PTFE as milky-white crystalline polymers and PMMA, PC, and PET as transparent amorphous polymers were used in measuring an impulse. The C_m of all the polymers examined here exceeded the maximum value obtained with aluminum, 18 μNs/J. By fitting the C_m equation to the experimental result, the effective absorption coefficient during laser ablation was estimated to be three to six orders of magnitude larger than that without ablation. The maximum C_m, 66 μNs/J, was obtained by PTFE with an effective absorption coefficient more than six times smaller than that of the other polymers.

These results will be essential when applying the laser ablation propulsion technique in future missions in space such as space debris deorbiting or de-tumbling, space transportation, and satellite attitude or orbital control using high repetitive 1 μm laser pulses, which is obtained by diode and fiber lasers.

Acknowledgments

はじめに、指導教官である衝撃波・宇宙推進研究グループ 佐宗章弘教授に感謝の意を表します。企業を退社し、何の実績もなかった私を受け入れてくださいました。恵まれた環境で研究を行わせて下さったことに加え、リーディング大学院のメンター補佐やRAを紹介していただけるなど金銭的な面も気にかけていただきました。また、数えきれないミーティングを通して、研究結果の物理的な解釈や意義について、さらには研究に対して一切妥協しない姿勢を学ばせていただきました。また、本論文作成にあたり、審査員として多くのご助言をいただきました、笠原次郎教授、堀澤秀之教授、森浩一准教授には深く感謝いたします。

また、鳥取大学 酒井武治教授、筑波大学 横田茂准教授、衝撃波・宇宙推進研究グループ 岩川輝講師には数々のご助言を賜りここに謝意を表します。

装置の作成にあたり、名古屋大学技術部の皆様、特に齋藤彰氏には加工作業や加工ノウハウについて数多くのご助言を賜りました。

実験の遂行に当たり王彬博士からは数多くの助言をいただくと共に、日々研究に関する議論に付き合っていただいたことに感謝いたします。これらの助言および議論は一連の研究を遂行するのに必要不可欠でした。

また、第4章はOskar Dondelewski君が実験に多大なる貢献をしているものであり、また、片桐佑介君が事前調査や実験準備を手伝ったものであり、ここに謝意を表します。

また、私が在籍した2011年10月から2017年3月の間に研究室に所属していた学生、また研究室以外で関わりのあった学生全員に対し感謝の意を述べると共に将来の活躍を祈念致します。

最後に、ここまで私を育ててくれた祖父母と、父、母、兄、そして陰ながら支えてくれた妻に特別の謝意を表します。

References

[1] D. Kessler, N. Johnson, The Kessler Syndrome: Implications to Future Space Operations, 33rd Annu. AAS Guid. Control Conf. (2010) 1–15.

[2] S. Karg, S. Scharring, H. Eckel, Laser ablation investigations for future microthrusters, AIP Conf. Proc. (2012).

[3] L.W. Swanson, Liquid metal ion sources: Mechanism and applications, Nucl. Instruments Methods Phys. Res. 218 (1983) 347–353.

[4] M. Tajmar, A. Genovese, W. Steiger, Indium Field Emission Electric Propulsion Microthruster Experimental Characterization, J. Propuls. Power. 20 (2004) 211–218.

[5] M. Tajmar, C. Scharlemann, A. Genovese, N. Buldrini, W. Steiger, I. Vasiljevich, Liquid-metal-ion source development for space propulsion at ARC, Ultramicroscopy. 109 (2009) 442–446.

[6] Koizumi, H., Study on Micro Space Propulsion, doctoral dissertation, 2006.

[7] G.A. Landis and F. Hrach, Satellite relocation by tether deployment. NASA Technical Memo 101992 (1989). See also G. A. Landis, Vision-21: Space Travel for the Next Millenium, NASA Conference Proceedings, CP-10059 (1990).

[8] R.D. Estes, E.C. Lorenzini, J. Sanmart-egrave, N, J. Pel-Uuml, Ez, M. Mart-egrave, nez-S-Uuml, Nchez, C.L. Johnson, I.E. Vas, Bare Tethers for Electrodynamic Spacecraft Propulsion, J. Spacecr. Rockets. 37 (2000) 205–211.

[9] C.R. Phipps, M. Birkan, W. Bohn, H.-A. Eckel, H. Horisawa, T. Lippert, M. Michaelis,

Y. Rezunkov, A. Sasoh, W. Schall, S. Scharring, J. Sinko, Review: Laser-Ablation Propulsion, J. Propuls. Power. 26 (2010) 609–637.

[10] Y. Rezunkov, A. Safronov, A. Ageichik, M. Egorov, V. Stepanov, V. Rachuk, V. Guterman, A. Ivanov, S. Rebrov, and A. Golikov, Performance Characteristics of Laser Propulsion Engine Operating Both in CW and Repetitively Pulsed Modes, Proceedings of the Fourth International Symposium on Beamed Energy Propulsion, AIP Conference Proceedings, American Inst. of Physics, Melville, NY, 830 (2006) 3-13.

[11] C.R. Phipps, J. Luke, Diode laser-driven microthrusters - a new departure for micropropulsion, AIAA J. 40 (2002) 310–318.

[12] C.R. Phipps, J.R. Luke, W. Helgeson, R. Johnson, Performance test results for the laser-powered microthruster, in: AIP Conf. Proc., 2006: pp. 224–234.

[13] C.R. Phipps, J.R. Luke, T. Lippert, M. Hauer, a. Wokaun, Micropropulsion using laser ablation, Appl. Phys. A. 79 (2004) 1385–1389.

[14] C.R. Phipps, J. Luke, W. Helgeson, 3ks Specific Impulse with a ns-pulse Laser Microthruster, 298 (2005).

[15] D.A. Gonzales, and R.P. Baker, Micropropulsion using a Nd:YAG microchip laser, in High-Power Laser Ablation IV, edited by C. R. Phipps, Proceedings of SPIE 4760, SPIE, Taos, NM, USA, (2002) 752–765

[16] J. Ziemer, Laser ablation microthruster technology, 33rd Plasmadynamics Lasers Conf. (2002).

[17] S. Kawamoto, T. Makida, F. Sasaki, Y. Okawa, S. Nishida, Precise numerical simulations of electrodynamic tethers for an active debris removal system, Acta Astronaut. 59

(2006) 139–148.

[18] S. Nishida, S. Kawamoto, Y. Okawa, F. Terui, S. Kitamura, Space debris removal system using a small satellite, Acta Astronaut. 65 (2009) 95–102.

[19] K. Wormnes, R. Le Letty, L. Summerer, H. Krag, R. Schonenborg, O. Dubois-Matra, E. Luraschi, J. Delaval, A. Cropp, ESA technologies for space debris remediation, 6th Eur. Conf. Sp. Debris. (2013) 1–2.

[20] J.C. Liou, An active debris removal parametric study for LEO environment remediation, Adv. Sp. Res. 47 (2011) 1865–1876.

[21] J.-C. Liou, N.L. Johnson, A sensitivity study of the effectiveness of active debris removal in LEO, Acta Astronaut. 64 (2009) 236–243.

[22] J.-C. Liou, Collision activities in the future orbital debris environment, Adv. Sp. Res. 38 (2006) 2102–2106.

[23] C.R. Phipps, G. Albrecht, H. Friedman, D. Gavel, E.V. George, J. Murray, C. Ho, W. Priedhorsky, M.M. Michaelis, J.P. Reilly, ORION: Clearing near-Earth space debris using a 20-kW, 530-nm, Earth-based, repetitively pulsed laser, Laser Part. Beams. 14 (1996) 1.

[24] W. O. Schall, Removal of small space debris with orbiting lasers, Proc. SPIE 3343, High-Power Laser Ablation, 564 (1998).

[25] R. Soulard, M.N. Quinn, T. Tajima, G. Mourou, ICAN: A novel laser architecture for space debris removal, Acta Astronaut. 105 (2014) 192–200.

[26] T. Ebisuzaki, M.N. Quinn, S. Wada, L.W. Piotrowski, Y. Takizawa, M. Casolino, M.

Bertaina, P. Gorodetzky, E. Parizot, T. Tajima, R. Soulard, G. Mourou, Demonstration designs for the remediation of space debris from the International Space Station, Acta Astronaut. 112 (2015) 102–113.

[27] See http://akagi.nuae.nagoya-u.ac.jp/en/ for a moving image of "Stop Rotation of Debirs by Laser Ablation" (last accessed November 7, 2016).

[28] C. Phipps, J. Luke, D. Funk, D. Moore, J. Glownia, T. Lippert, Laser impulse coupling at 130fs, Appl. Surf. Sci. 252 (2006) 4838–4844.

[29] C.R. Phipps, T.P. Turner, R.F. Harrison, G.W. York, W.Z. Osborne, G.K. Anderson, X.F. Corlis, L.C. Haynes, H.S. Steele, K.C. Spicochi, T.R. King, Impulse coupling to targets in vacuum by KrF, HF, and CO_2 single-pulse lasers, J. Appl. Phys. 64 (1988) 1083–1096.

[30] A. V Pakhomov, M.S. Thompson, W. Swift, D.A. Gregory, Ablative laser propulsion - Specific impulse and thrust derived from force measurements, AIAA J. 40 (2002) 2305–2311.

[31] D'Souza, B.C., Development of Impulse Measurement Techniques for the Investigation of Transient Forces Due to Laser-Induced Ablation, Dissertation, 2007.

[32] A.A. Puretzky, D.J. Styers-Barnett, C.M. Rouleau, H. Hu, B. Zhao, I.N. Ivanov, D.B. Geohegan, Cumulative and continuous laser vaporization synthesis of single wall carbon nanotubes and nanohorns, Appl. Phys. A. 93 (2008) 849–855.

[33] F. Colao, V. Lazic, R. Fantoni, S. Pershin, A comparison of single and double pulse laser-induced breakdown spectroscopy of aluminum samples, Spectrochim. Acta Part B. 57 (2002) 1167–1179.

[34] K. Mori, A. Sasoh, Preheating Technique to Enhance the Laser Ablation Impulse from, 3 (2011).

[35] J.E. Sinko, N.B. Dhote, J.S. Lassiter, D. a. Gregory, Conical nozzles for pulsed laser propulsion, Proc. SPIE. 7005 (2008) 1-10.

[36] K. Suzuki, K. Sawada, R. Takaya, A. Sasoh, Ablative Impulse Characteristics of Polyacetal with Repetitive CO_2 Laser Pulses, J. Propuls. Power. 24 (2008) 834–841.

[37] P. Solana, P. Kapadia, J.M. Dowden, P.J. Marsden, An analytical model for the laser drilling of metals with absorption within the vapour, J. Phys. D. Appl. Phys. 32 (1999) 942–952.

[38] A. Sasoh, Laser-driven in-tube accelerator, Rev. Sci. Instrum. 72 (2001) 1893–1898.

[39] V. Srinivasan, M.A. Smrtic, S. V. Babu, Excimer laser etching of polymers, J. Appl. Phys. 59 (1986) 3861–3867.

[40] J.E. Sinko, C.R. Phipps, Modeling CO_2 laser ablation impulse of polymers in vapor and plasma regimes, Appl. Phys. Lett. 95 (2009) 13–15.

[41] L. Urech, T. Lippert, C.R. Phipps, A. Wokaun, Polymer ablation: From fundamentals of polymer design to laser plasma thruster, Appl. Surf. Sci. 253 (2007) 6409–6415.

[42] T. Lippert, M. Hauer, C.R. Phipps, a Wokaun, Fundamentals and applications of polymers designed for laser ablation, Appl. Phys. A Mater. Sci. Process. 77 (2003) 259–264.

[43] P. Willis, C.H. Hsieh, Space Applications of Polymeric Materials, Kobunshi, 49 (2000) 52–56.

[44] C.R. Phipps, A laser-optical system to re-enter or lower low Earth orbit space debris, Acta Astronaut. 93 (2014) 418–429.

[45] J.C. Liou, An active debris removal parametric study for LEO environment remediation, Adv. Sp. Res. 47 (2011) 1865–1876.

[46] C.R. Phipps, R.F. Harrison, T. Shimada, G.W. York, T.P. Turner, X.F. Corlis, H.S. Steele, L.C. Haynes, T.R. King, Enhanced vacuum laser-impulse coupling by volume absorption at infrared wavelengths, Laser Part. Beams. 8 (1990) 281–298.

[47] W. Schall, H. Eckel, J. Tegel, F. Waiblinger, S. Walther, Properties of laser ablation products of Delrin with CO_2 laser, DLR FA8655-03-1-3061, (2004).

[48] S. Scharring, E. Wollenhaupt, H.-A. Eckel, H.-P. Röser, C. Phipps, K. Komurasaki, J. Sinko, Flight Experiments On Energy Scaling For In-Space Laser Propulsion, (2010) 326–337.

[49] L. N. Myrabo, D. G. Messitt, F. B. Mead, Jr.: Ground and Flight Tests of a Laser Propelled Vehicle, 36th AIAA Aerospace Science Meeting and Exhibit, AIAA Paper 98-1001, Reno, NV, 12– 15 Jan. 1998.

[50] H. Tsuruta, B. Wang, Z. Wang, S. Yokota, A. Sasoh, Repetitive Pulse Performance of One-Micrometer Laser-Ablation Propulsion onto Aluminum, J. Propuls. Power. 30 (2014) 1485–1489.

[51] S. Amoruso, M. Armenante, Absorption and saturation mechanisms in aluminium laser ablated plasmas, Appl. Phys. A. 65 (1997) 265–271.

[52] N.M. Shaikh, S. Hafeez, B. Rashid, M. a. Baig, Spectroscopic studies of laser induced aluminum plasma using fundamental, second and third harmonics of a Nd:YAG laser, Eur. Phys. J. D. 44 (2007) 371–379.

[53] F. Caridi, L. Torrisi, D. Margarone, a. Picciotto, a. M. Mezzasalma, S. Gammino, Energy distributions of particles ejected from laser-generated pulsed plasmas, Czechoslov. J.

Phys. 56 (2006) B449–B456.

[54] C.R. Phipps, J. Luke, Laser Ablation and its Applications, Laser Space Propulsion, Springer (2007) 407 –434.

[55] B. D'souoza, Development of Impulse Measurement Techniques for the Investigation of Transient Forces due to Laser-Induced Ablation, Faculty of the Graduate School University of Southern California, (2007).

[56] B. D'Souza, A. Ketsdever, Direct Impulse Measurements of Ablation Processes from Laser-Surface Interactions, 36th AIAA Plasmadynamics Lasers Conf. (2005).

[57] K. Anju, K. Sawada, A. Sasoh, K. Mori, E. Zaretsky, Time-Resolved Measurements of Impulse Generation in Pulsed Laser-Ablative Propulsion, J. Propuls. Power. 24 (2008) 322–329.

[58] E. Carpene, D. Höche, P. Schaaf, Fundamentals of Laser-Material Interactions, in: P. Schaaf (Ed.), Laser Processing of Materials – Fundamentals, Applications and Developments, Springer, New York, 2010, pp. 21-47.

[59] M. Makropoulou, A.A. Serafetinides, C.D. Skordoulis, Ultra-violet and infra-red laser ablation studies of biocompatible polymers, Lasers Med. Sci. 10 (1995) 201–206.

[60] J.E. Sinko, Vaporization and Shock Wave Dynamics for Impulse Generation in Laser Propulsion, *Dissertation*, 2008.

[61] T. Yamanaka, Plasma Production by Laser, J. Plasma Fusion Res. 69 (1993) 656–662.

Published papers related to this dissertation

Chapter 3, Section 3.1

H. Tsuruta, B. Wang, Z. Wang, S. Yokota, A. Sasoh, Repetitive Pulse Performance of One-Micrometer Laser-Ablation Propulsion onto Aluminum, J. Propuls. Power. 30 (2014) 1485–1489.

Chapter3, Sections 3.2 and 3.3

H. Tsuruta, B. Wang, Z. Wang, A. Sasoh, Influence of Microscopic Crater Formation on Impulse Generated with Repetitive Pulsed Laser Ablation, Trans. JSASS Aerosp. Tech. Japan. 13 (2015) 33–36.

Chapter 4

H. Tsuruta, O. Dondelewski, Y. Katagiri, B. Wang, A. Sasoh, Ablation spot area and impulse characteristics of polymers induced by burst irradiation of 1 μm laser pulses, Acta Astronaut. 136 (2017) 46–54.